arXiv:1411.3830v1 [astro-ph.GA] 14 Nov 2014

The Importance of the Magnetic Field from an SMA-CSO-Combined Sample of Star-Forming Regions

Patrick M. Koch[1], Ya-Wen Tang[1], Paul T. P. Ho[1,2], Qizhou Zhang[2], Josep Miquel Girart[3], Huei-Ru Vivien Chen[4,1], Pau Frau[5], Hua-Bai Li[6], Zhi-Yun Li[7], Hau-Yu Baobab Liu[1], Marco Padovani[8,9], Keping Qiu[10] , Hsi-Wei Yen[1], How-Huan Chen[2], Tao-Chung Ching[2,4], Shih-Ping Lai[4,1] and Ramprasad Rao[11]

pmkoch@asiaa.sinica.edu.tw

ABSTRACT

Submillimeter dust polarization measurements of a sample of 50 star-forming regions, observed with the Submillimeter Array (SMA) and the Caltech Submillimeter Observatory (CSO) covering pc-scale clouds to mpc-scale cores, are analyzed in order to quantify the magnetic field importance. The magnetic field misalignment δ – the local angle between magnetic field and dust emission gradient – is found to be a prime observable, revealing distinct distributions for sources where the magnetic field is preferentially aligned with or perpendicular to the source minor axis. Source-averaged misalignment angles $\langle|\delta|\rangle$ fall into systematically different ranges, reflecting the different source-magnetic field configurations. Possible bimodal $\langle|\delta|\rangle$-distributions

[1]Academia Sinica, Institute of Astronomy and Astrophysics, Taipei, Taiwan

[2]Harvard-Smithsonian Center for Astrophysics, 60 Garden Street, Cambridge, MA 02138, USA

[3]Institut de Ciències de l'Espai, CSIC-IEEC, Campus UAB, Facultat de Ciències, C5p 2, 08193 Bellaterra, Catalonia

[4]Institute of Astronomy and Department of Physics, National Tsing Hua University, 101 Section 2 Kuang Fu Road, Hsinchu 30013, Taiwan

[5]Observatorio Astronómico Nacional, Alfonso XII, 3 E-28014 Madrid, Spain

[6]Department of Physics, The Chinese University of HongKong

[7]Department of Astronomy, University of Virginia, P.O. Box 400325, Charlottesville, VA 22904, USA

[8]Laboratoire Univers et Particules de Montpellier, UMR 5299 du CNRS, Université de Montpellier II, place E. Bataillon, cc072, 34095 Montpellier, France

[9]INAF–Osservatorio Astrofisico di Arcetri, Largo E. Fermi 5, 50125 Firenze, Italy

[10]School of Astronomy and Space Science, Nanjing University, 22 Hankou Road, Nanjiing 210093, China

[11]Academia Sinica, Institute of Astronomy and Astrophysics, 645 N. Aohoku Place, Hilo, HI 96720, USA

are found for the separate SMA and CSO samples. Combining both samples broadens the distribution with a wide maximum peak at small $\langle|\delta|\rangle$-values. Assuming the 50 sources to be representative, the prevailing source-magnetic field configuration is one that statistically prefers small magnetic field misalignments $|\delta|$. When interpreting $|\delta|$ together with a magnetohydrodynamics force equation, as developed in the framework of the polarization-intensity gradient method, a sample-based log-linear scaling fits the magnetic field tension-to-gravity force ratio $\langle\Sigma_B\rangle$ versus $\langle|\delta|\rangle$ with $\langle\Sigma_B\rangle = 0.116 \cdot \exp(0.047 \cdot \langle|\delta|\rangle) \pm 0.20$ (mean error), providing a way to estimate the relative importance of the magnetic field, only based on measurable field misalignments $|\delta|$. The force ratio Σ_B discriminates systems that are collapsible on average ($\langle\Sigma_B\rangle < 1$) from other molecular clouds where the magnetic field still provides enough resistance against gravitational collapse ($\langle\Sigma_B\rangle > 1$). The sample-wide trend shows a transition around $\langle|\delta|\rangle \approx 45°$. Defining an effective gravitational force $\sim 1 - \langle\Sigma_B\rangle$, the average magnetic-field-reduced star-formation efficiency is at least a factor of two smaller than the free-fall efficiency. For about one forth of the sources the average efficiency drops to zero. The force ratio Σ_B can further be linked to the normalized mass-to-flux ratio, yielding an estimate for the latter one without the need of field strength measurements. Across the sample, a transition from magnetically supercritical to subcritcal is observed with growing misalignment $\langle|\delta|\rangle$.

Subject headings: ISM: clouds — ISM: magnetic fields, polarization — Methods: polarization

1. Introduction

Magnetic fields and their role in star formation have long been studied in the literature (e.g., Crutcher 2012; McKee & Ostriker 2007; Shu et al. 2006, 2004). Polarization observations in the optical, infrared and submillimeter bands often routinely detect extended polarized emission, revealing magnetic field morphologies across entire star-forming regions. While the higher-frequency optical / near-infrared light is polarized as a result of scattering off dust grains (e.g., Santos et al. 2014; Pereyra & Magalhães 2008), the submillimeter wavelengths directly show the emitted polarized light from dust. The grains are thought to be aligned with their shorter axes parallel to the magnetic field lines in most situations, thus emitting in a plane perpendicular to the field lines (Cudlip et al. 1982; Hildebrand et al. 1984; Hildebrand 1988; Lazarian 2007; Andersson 2012). Many submillimeter facilities have developed their polarization capabilities. Operating at a wavelengths $\lambda \sim 350\mu$m, Hertz on the Caltech Submillimeter Observatory (CSO) mapped magnetic fields in star-formation regions with a resolution of about $20''$. A summary

catalog with 56 sources is given in Dotson et al. (2010). Its successor instrument, SHARP (Li et al. 2008), is currently being operated on the CSO, achieving a resolution of about 10″. Dust continuum polarization was also observed with SCUPOL on the James Clerk Maxwell Telescope (JCMT) at $\lambda \sim 850\mu$m with a binned resolution of about 9″, summarized in the legacy catalog with 83 sources by Matthews et al. (2009). Higher-resolution maps are possible with interferometers. The Berkeley-Illinois-Maryland Association (BIMA) array reached about 2 -4″at 1.3 and 3.3 mm (Rao et al. 1998; Lai et al. 2001, 2002). More recently, both the Combined Array for Research in Millimeter-wave Astronomy (CARMA) and the Submillimeter Array (SMA) presented results from legacy-type surveys toward 38 star-forming regions and cores (Hull et al. (2014), $\theta \sim 2.5''$, $\lambda \sim 1.3$mm) and 14 high-mass star-forming clumps (Zhang et al. (2014), $\theta \sim 1-3''$, $\lambda \sim 870\mu$m).

All these observations have in common that they often cover large enough areas (of polarized emission) such that connected patches of projected magnetic field orientations become visible. This is advantageous to investigate magnetic field morphologies. Consequently, several studies are making use of this in combination with other tracers such as outflows, larger scale magnetic field orientations or theoretical models. The class 0 low-mass protostar L1157-mm is found to have an hourglass morphology (from CARMA observations) that aligns both with its outflow and also with the larger scale field detected by SHARP (Stephens et al. 2013). The magnetic field in the dense clump IRAS 20126-4104 (SHARP, Shinnaga et al. (2012)) is both aligned with its bipolar outflow as well as the larger scale field from optical polarimetry data. A comparison with numerical simulations indicates a cloud rotation axis inclined by about 60° with respect to the magnetic field. A positive correlation between mean field orientations and both pseudo-disk symmetry axes and bipolar outflow axes is derived from seven class 0 protostars in Davidson et al. (2011) and Chapman et al. (2013) based on SHARP polarization detections, sampling $\sim 10,000$ AU scales. On smaller scales, Hull et al. (2014) find that a subset of their sources has consistent magnetic field orientations between the larger scale ($\sim 20''$, probed by single-dish submillieter telescopes) and the smaller scale ($\sim 2.5''$) magnetic fields from CARMA. This is interpreted as the magnetic field playing a role in regulating infall down to smaller scales ($\sim$ 1000 AU) in these sources. Bipolar outflows (CO 2-1 transition) in their sample of low-mass protostars seem to be randomly oriented with respect to the smaller scale fields (Hull et al. 2013, 2014), although there is a trend that low-polarization sources have their outflows perpendicular to small-scale fields, indicating that these fields might being wrapped by rotation (Hull et al. 2014). The SMA sample (Zhang et al. 2014) indicates that magnetic fields at dense core scales are either aligned within 40° of or perpendicular to the larger parsec-scale fields. Similar to the CARMA result, they also conclude that outflows (CO 3-2 transition) are randomly oriented with the core magnetic fields. Numerical simulations of collapsing cores, investigating scenarios to align / misalign rotation, outflows and magnetic fields are presented in e.g., Li et al. (2013); Krasnapolsky et al. (2012); Machida et al. (2011); Ciardi & Hennebelle (2010).

In ideal situations, magnetic field theoretical models and simulations can be fairly closely matched to polarization observations (e.g., Gonçalves et al. 2008; Frau et al. 2011; Kataoka et al. 2012). A mathematical model to fit an observed hourglass field morphology is derived in Ewertowski & Basu (2013). Their analytic formulae – assuming an axisymmetric purely poloidal field threading a flattened star-forming core and connecting to a uniform background field – are using the shape of the hourglass pattern to constrain the ratio of local-to-background magnetic field strength. Provided an independent measurement of the background field strength, local field strength values in a region of interest can be calculated from their analytic approach.

Many observed star-forming sources are, however, irregular and complicated. It is, thus, important and desirable to develop new techniques that can directly and independently extract information from detected polarization. A major shortcoming of dust polarization is that only sky-projected field morphologies (rotated by 90° from measured polarization orientations) are observed but no magnetic field strengths. Recent developments aiming at improving this situation include the polarization-angle dispersion function leading to an estimate of the turbulent-to-mean magnetic field strength (Hildebrand et al. 2009; Houde et al. 2009; Koch, Tang & Ho 2010; Houde et al. 2011; Poidevin et al. 2013), the study of turbulent velocity dispersion spectra of co-existing ions and molecules to constrain the ambipolar diffusion scale and the plane-of-sky component field strength (Hezareh et al. 2010; Li & Houde 2008) and the polarization-intensity gradient method to derive the local total magnetic field strength (Koch, Tang & Ho 2012a,b). In this work here, we focus on a previously introduced observable: the angle δ between the local magnetic field orientation and its underlying dust emission gradient orientation. Although not limited to dust polarization measurements, we focus on dust submillimeter observations across a large and diverse sample, with the goal to (1) illustrate characteristic features and differences in δ based on a to date largest sample of 50 sources, and (2) to provide an interpretation for δ via the polarization-intensity gradient method, illustrating clear trends in the importance of the magnetic field across the sample that are accessible via δ. This study is part of the program on the SMA (Ho et al. 2004) to investigate the structure of the magnetic field from large to small scales.

The paper is organized as follows. Section 2 briefly describes selection criteria and properties of the SMA and the CSO sample. The main observable – the angle δ – its interpretation and the polarization - intensity gradient method are summarized in Section 3, based on earlier results in Koch, Tang & Ho (2012a,b, 2013). Results for the angle δ follow in Section 4, starting from overall-sample to group and source-averaged results. Section 5 discusses interpretation and comparison with previous results. Conclusion and summary are given in Section 6.

2. Samples

This work combines data from two different samples and telescopes (Table 1). Hertz on the single-dish telescope CSO has published a catalog of polarization observations at a wavelength $\lambda \sim 350\mu$m with a resolution $\theta \sim 20''$ (Dotson et al. 2010). The SMA, operating in various array configurations at $\lambda \sim 870\mu$m, is sampling smaller scales with resolutions of a few arcseconds down to sub-arcsecond scales.

2.1. SMA

The SMA[1] has been pioneering high-resolution submillimeter polarization observations. Whereas the earliest observations were focusing on the most promising and brightest targets (e.g., Girart et al. 2006, 2009; Rao et al. 2009; Tang et al. 2009a,b; Chen et al. 2012; Tang et al. 2013), later receiver and correlator upgrades made it possible to also observe fainter sources. This has boosted the sample of high-resolution low-and high-mass star-forming regions which currently totals about 30 sources. A substantial number of these sources (14) was observed through a recent dedicated SMA polarization legacy program (Zhang et al. 2014), sampling star-forming clumps with densities larger than 10^5 cm^{-3} at scales around or smaller than 0.1 pc. Detailed follow-up source-by-source analyses are being conducted, with first results published for DR21(OH) (Girart et al. 2013), G192.16-3.84 (Liu et al. 2013), G35.2-0.74 N (Qiu et al. 2013). For our analysis here, we have applied selection criteria identical to the ones for the CSO sample: coherent polarization patches with at least 10 polarization segments, and a Stokes *I* continuum detection strong enough to define a gradient. Besides newly detected sources from the SMA polarization legacy program, the sample analyzed here also comprises some earlier observed targets (Table 1).

2.2. CSO

The CSO/Hertz polarization catalog contains 56 regions, mostly Galactic sources and some galaxies (Dotson et al. 2010)[2]. We chose a total of 27 sources from the CSO catalog. Sources are selected based on their coverage of detected polarized emission, together with the condition that the Stokes *I* continuum emission need to be strong enough to define a gradient. In order to have at least some connected patches, we request a minimum of 10 measured polarization – intensity

[1] The Submillimeter Array is a joint project between the Smithsonian Astrophysical Observatory and the Academia Sinica Institute of Astronomy and Astrophysics, and is funded by the Smithsonian Institution and the Academia Sinica.

[2] The publicly available reduced data can be found at http://iopscience.iop.org/0067-0049/186/2/406/fulltext/.

gradient pairs for our analysis. $|\delta|$-maps together with some basic statistical numbers for each of the CSO-selected sources are given in Koch, Tang & Ho (2013).

3. Analysis Technique: Observable δ and Polarization - Intensity Gradient Method

The local angle δ is measured between a magnetic field orientation and a dust emission gradient (Figure 1). In our study here, an observed dust polariztion orientation which is then rotated by 90° reveals the magnetic field orientation. Nevertheless, any measurement showing the magnetic field morphology, as e.g., line polarization, Faraday rotation or Zeeman splitting, can be used and what follows is generally applicable. δ is uanambiguously defined in the range 0 to +90° (as the smaller of the two angles complementary to 180°), or –90° to +90° when giving it a sense of orientation. δ is straighforward to derive from an observation. A simple inspection by eye can often distinguish between zones of small (prevailing field orientation rather orthogonal to emission contours) and zones of large δ (prevailing field orientation rather parallel to contours).

What is the meaning of the angle δ? With the help of an ideal magnetohydrodynamics (MHD) force equation, by decomposing the magnetic field orientation in an orthonormal system with unity vectors parallel and normal to an emission contour (Figure 1), the angle $|\delta|$ with $\sin|\delta| \in [0,1]$ quantifies the fraction of the available magnetic field tension force along a density gradient direction[3] (Koch, Tang & Ho 2013). Thus, $|\delta|$ can be interpreted as a magnetic field alignment deviation or efficiency that measures how the magnetic field is responsible for an observed density morphology along the gradient direction. Magnetic field lines closely aligned with density gradients, as e.g., seen in polar regions in collapsing systems, yield $|\delta| \approx 0$ or small, which indicates that the magnetic field tension force is not or only minimally slowing down infall in this region along the density gradient direction. Contrary to that, in regions where the magnetic field is more bent, as e.g., in the inner part of an accretion plane where the field becomes close to orthogonal to a density gradient, $|\delta|$ is significantly larger than 0. Hence, the field tension force can maximally inhibit collapse or any motion along the density gradient direction. Therefore, $|\delta|$-maps contain information on the role of the magnetic field (Koch, Tang & Ho 2013). Changes in $|\delta|$ across a star-formation region can reveal zones of major or minor magnetic field influence. Additionally, many sources reveal bimodal distributions in δ when giving it a sense of orientation, i.e., when differentiating

[3] Observed emission – generally a combined result of density and temperature – does not directly correspond to the density as used in the MHD force equation. This is, nevertheless, not of a concern, because our approach involves the orientation of the gradient of emission or density. A constant temperature, steep or gentle temperature gradients that align with a density gradient will all lead to emission gradient orientations that can be identified (in orientation) with the MHD density gradient orientation. Only a significant temperature gradient that deviates a lot in direction from a density gradient could be problematic.

between a field line rotated clockwise or counter-clockwise with respect to an emission gradient. This can be interpreted as signs of a collapse (or the beginning of a collapse) which will start to bend initially straight magnetic field lines along the accretion direction that subsequently leads to $+/-\delta$ above and below the accretion plane (Koch, Tang & Ho 2013).

We note that δ and its characteristic features, found across a sample of about 30 sources in Koch, Tang & Ho (2013), are based entirely on observations only. In order to further quantitatively assess the magnetic field, some of the observational results in the following sections will be further analyzed with the polarization-intensity gradient method (Koch, Tang & Ho 2012a). At every position of detected polarization, this method leads to a local magnetic field strength and a ratio between the local field tension force and gravity. The background of this method is the ideal MHD force equation, making use of the misalignment angle $|\delta|$. In a molecular cloud, the interaction of all the forces (magnetic field, gravity, pressure gradients) leads to the observed magnetic field and dust morphologies. Hence, these forces leave a geometrical imprint, like the misalignment angle $|\delta|$, that can be identified with the various terms in the MHD force equation. In particular, the direction of the field tension force is orthogonal to the detected field orientation (i.e., parallel to the detected dust polarization orientation), a field curvature can be derived from adjacent field segments, the direction of the local gravitational pull can be calculated by summing up all the surrounding mass. With this, a force triangle can be constructed at every location of detected polarization. This triangle can be closed and solved for the local field strength under the approximation that the orientation of the emission gradient is a measure for the inertial term in the MHD force equation. By taking additionally into account velocity bulk directions, this approximation was further studied in Koch, Tang & Ho (2013) and confirmed to be robust for field strength and force ratio estimates. The resulting local field strength is given by (Koch, Tang & Ho 2012a):

$$B = \sqrt{\frac{\sin\psi}{\sin\left(\frac{\pi}{2}-|\delta|\right)}(\nabla P + \rho\nabla\phi)4\pi R}, \tag{1}$$

where $\rho\nabla\phi$ and ∇P are the gravitational pull and pressure gradient, and ψ is the difference in orientation between the local gravitational pull and/or pressure gradient and the emission gradient (Figure 1). ρ is the density and R is the magnetic field radius. It is important to remark that this method provides a total magnetic field strength. With the field tension force $F_B = B^2/(4\pi R)$, the above equation can be rewritten as:

$$\Sigma_B \equiv \frac{\sin\psi}{\sin\left(\frac{\pi}{2}-|\delta|\right)} = \frac{F_B}{|F_G + F_P|}, \tag{2}$$

where F_G and F_P are gravitational pull and any possible additional pressure gradient. Σ_B quantifies how significant the local field tension force is, as compared to the other forces. Interestingly, this ratio is free of any molecular cloud model assumptions and only relies on two measurable angles

that reflect the geometrical imprint of magnetic field and other forces. Assuming pressure gradients to be typically small[4] compared to gravity in our samples, Σ_B provides a criterion whether local collapse is possible ($\Sigma_B < 1$) or whether the field tension is large enough to inhibit local collapse ($\Sigma_B > 1$). Σ_B-maps of molecular clouds systematically show zones of smaller- or larger-than-one Σ_B-values. The same transition can often also be observed in $|\delta|$-maps which makes them an easy tracer for changes in the field significance. $|\delta|$- and Σ_B-maps for each of the CSO-selected sources (Section 2.2 and Table 1) are given in Koch, Tang & Ho (2013). Finally, both Σ_B and B are little or not at all affected by projection effects. This is possible because the projection correction enters as a ratio of two inclination angles (for ψ and $|\delta|$). For identical inclination angles for magnetic field line and emission gradient, the projection effect cancels out. The projection effect is negligible or less than 30% as long as one inclination angle is within 45° and the other one is not more than 50° different from the first one (Koch, Tang & Ho 2012a).

4. Results

This section starts by presenting SMA-CSO-combined overall results (Section 4.1). This is followed by a refined analysis where sources from the combined samples are categorized based on proposed criteria (Section 4.2). Finally, Section 4.3 looks into averaged source-by-source trends and compares them to the proposed categorization from Section 4.2. Results for both all independent δ, ψ and Σ_B, and also for their source-averaged quantities $\langle\cdots\rangle$ are shown.

---

[4] Thermal pressure is balancing gravity following $GM/R_c \sim k_B T/m$ where M, R_c and T are the molecular cloud mass, radius and temperature. m is related to the cloud gas composition and proportional to the hydrogen mass, $m \sim m_H$, with a numerical factor of order unity. For pure thermal support, this leads to $R_c \approx 0.1(M/M_\odot)(10K/T)$pc. The sources in our samples comprise hundreds up to thousands of solar masses. This leads to thermally supported length scales of ∼10 pc or larger. Our largest observed scales in the CSO sample are about 1 pc, with most of the sources being observed on scales of $\sim 10-100$ mpc. Thus, we are very likely sampling sufficiently small scales where thermal pressure is small and negligible compared to gravity. This also still holds if the molecular cloud temperature is higher with T ∼20-30 K. Yet an additional pressure gradient can result from large-scale flows. Compressive flows are suggested to contribute to and shape observed filamentary networks with coherent structures on pc- or larger scales (e.g., Peretto et al. 2012; André et al. 2013). Significant pressure gradients might be present here, in particular for supersonic flows and turbulence. Omitting such gradients can lead to uncertainties in our analysis. This shortcoming can be overcome if additional large-scale velocity information is available overlapping with polarization data. The sample analyzed here, however, is again probing mostly smaller scales which likely eliminates a possibly significant bias from large-scale converging flows. Finally, pressure from turbulence with velocity v_T scales as $v_T^2 \sim k_B T/m$. With typical velocity dispersions of $\sim 1-2$ km/s in our sample, gravity is also dominating over turbulent pressure on scales of ~ 1 pc and smaller.

4.1. Overall Sample

We start by looking for general overall trends, based on the combined full SMA-CSO sample. Here, we intentionally do not distinguish between SMA and CSO sources or any further source properties because we are aiming at characterizing the magnetic field in any star-forming region. To this purpose, we show for all sources with all their detected polarization orientations, their angles $|\delta|$ with their corresponding Σ_B-values (Figure 2). For the total of 50 sources, this amounts to close to 4,000 independent $(|\delta|, \Sigma_B)$-pairs. This scatter plot clearly traces and follows an upper envelope which is determined by the maximum possible Σ_B-values which are $max\,\Sigma_B = 1/\sin\alpha \geq 1$ for $\sin\psi \equiv 1$. The combined sample fills the entire possible range in $|\delta|$ with a distribution displaying a broad peak around smaller $|\delta|$-values with a slow roll-off and an extended tail towards larger values (lower panel in Figure 7). Binning $|\delta|$ into intervals of 10° shows uniform $|\delta|$-distributions with gradually fewer data points in subsequent bins towards larger $|\delta|$-values. The distributions of Σ_B show broad peaks around Σ_B-values initially smaller than 1. These peaks broaden in subsequent $|\delta|$ bins and shift eventually toward Σ_B-values larger than 1. At this point here, no distinction is made between individual sources. As we will discuss in the Sections 4.2 and 4.3, distinct source types preferentially fall into distinct zones in the scatter plot in Figure 2. Filling the entire possible ranges in $|\delta|$ and Σ_B possibly indicates that we might have a fairly complete and unbiased sample representing all possible source types. We stress that it is not automatically obvious from the beginning that the scatter plot (Figure 2) needs to show a complete (though not uniform) coverage. This is not obvious because the force ratio $\Sigma_B = \sin\psi/\sin\alpha$ allows for a vast range of Σ_B-values within $[0, \infty)$. In particular, values could be exclusively always smaller than 1, or they could be always ≥ 1. Nevertheless, values cover a range across the dividing line $\Sigma_B = 1$. While a single angle $|\delta|$ can be affected by projection effects due to its unknown inclination angle, for a large number of more than 1,000 independent data points projection effects are likely averaging out. The binned uniform $|\delta|$-distributions together with the gradually broadening Σ_B-distributions suggest that, generally on average, larger $|\delta|$-values point toward larger Σ_B-values. And indeed, $|\delta|$-values averaged for all the binned intervals confirm this. Furthermore, the binned values follow approximately the curve $\sim 1/2 \cdot 1/\sin\alpha$ (Figure 2), which is simply the mean between 0 and $max\,\Sigma_B = 1/\sin\alpha$.

In conclusion, for a large sample without further distinguishing any individual sources, we find a sample-wide trend where growing $|\delta|$-values indicate growing Σ_B-values following $\Sigma_B \approx 1/2 \cdot 1/\sin(\pi/2 - |\delta|)$. On average, gravity is balanced by the magnetic field tension force, i.e., $\Sigma_B \equiv 1$, for $|\delta| = 60°$. Individual sources or groups of sources can still reveal different properties (Section 4.2 and 4.3).

4.2. Source Categorization

Koch, Tang & Ho (2013) proposed a scenario with an evolutionary magnetic field role which leaves its imprints in the angle $|\delta|$. Two distinct intermediate phases are identified (Table 2): sources of type IIA (with their magnetic field roughly perpendicular to the cloud major axis), and sources of type IIB (with their magnetic field roughly parallel to the cloud major axis). This categorization was motivated by the very clear examples of Mon R2 (IIA) and M+0.25+0.01 (IIB) from the CSO catalog (Dotson et al. 2010). Additional sources from the CSO sample were then tentatively categorized in Table 2 in Koch, Tang & Ho (2013). For completeness, an extended version of this table including the new SMA sources is reproduced here (Table 1). Since we are also interested in inter-sample differences (between the SMA and the CSO) we show results here separately for the two instruments. The top row in Figure 3 shows $|\delta|$-histograms for all the sources that are (clearly) identified as IIA and IIB. This includes 12 IIA and 7 IIB sources from the CSO sample and 9 IIA and 4 IIB sources from the SMA sample. The remaining sources are discarded because of their less complete and/or less clear polarization patterns[5]. Individual source-based histograms in Appendix B in Koch, Tang & Ho (2013) for the CSO sample were already hinting differences in distributions (which was an additional motivation for the classification scheme). The group-based histograms now reveal a very clear difference with a falling distribution with $\langle|\delta|\rangle_{IIA} = 34^\circ$ (SMA) and 30° (CSO), and an opposite trend with a growing distribution with $\langle|\delta|\rangle_{IIB} = 51^\circ$ (SMA) and 51° (CSO). As an obvious consequence, a Kolmogorov-Smirnov (KS) test rejects the null hypothesis (i.e., probability p that the two samples IIA and IIB originate from an identical distribution) with $p \sim 10^{-15}$ (SMA) and $p \sim 10^{-37}$ (CSO), where the maximum deviations (k-value) between their cumulative distributions are $k = 0.34$ (SMA) and $k = 0.42$ (CSO). An inter-sample KS test, i.e., IIA_{SMA} versus IIA_{CSO} and IIB_{SMA} versus IIB_{CSO}, gives $p \sim 10^{-4}$ and $k = 0.10$ for IIA and $p = 0.94$ and $k = 0.05$ for IIB. We can, thus, conclude that equal-type distributions from two different instruments show a much closer resemblance than distributions from different types from the same instrument, with IIB-type sources even showing a high probability to reflect identical distributions. This is intriguing because this indicates that the sampling of different scales and densities by the SMA and the CSO is less relevant in the context here. Independent of that, both instruments seem to reveal the same different types of morphologies. This can also be seen from the cumulative distributions in column 5 in Figure 3. The last column shows the results for 5 type-III[6] sources from the SMA sample. No type-III sources are found in the CSO sample. The $|\delta|$-distribution shows an even more pronounced peak towards small values with $\langle|\delta|\rangle \approx 30^\circ$.

---

[5] Table 1 still lists an attempted tentative categorization for all the sources in both samples.

[6] Evolving from the more elongated structures of IIA- and IIB-type sources, the later type-III sources are less elongated, but more symmetrized as gravity starts to pull in the magnetic field lines (Koch, Tang & Ho 2013).

Besides the angle $|\delta|$, the Stokes I integrated dust emission is another prime observable that reflects mass and morphology in the star-forming regions. Since every source has a different absolute flux emission, a peak-normalized emission, $I_{norm} \in [0, 1]$, is used in order to compare emission distributions across samples. The third row in Figure 3 displays histograms of I_{norm} for IIA and IIB in the SMA and CSO samples. For these distributions, the normalized Stokes I emission only at the positions of detected polarized emission (where $|\delta|$ is identified) is used. As it is evident from the two CSO panels, the I_{norm}-histograms for IIA and IIB are very different among the CSO sample: the IIA-group shows an exponential-like fall off toward the stronger emission end, whereas type-IIB sources reveal a broader distribution in I_{norm} with a more gentle decrease with brighter emission. A KS test again clearly discriminates between the two distributions ($p \sim 10^{-22}$, $k = 0.29$). The mean normalized emissions are $\langle I_{norm} \rangle_{IIA} = 0.28$ and $\langle I_{norm} \rangle_{IIB} = 0.44$. The observed Stokes I emission is an integrated and projected quantity. Nevertheless, the clear difference in distributions between IIA and IIB is likely pointing to some underlying differences in morphology; e.g., IIB CSO sources show more abundant brighter areas than IIA sources, which could be a consequence of flatter or steeper density profiles. All SMA types (IIA, IIB, III) show exponential-like fall offs where all average values are around 0.30. All the SMA distributions are fairly similar to the CSO-IIA distribution, leaving only the CSO-IIB distribution as clearly distinct (blue dashed line in the cumulative distribution plot in the third row.

With the clear segregation in $|\delta|$, the magnetic field seems a plausible candidate to explain these. Therefore, we proceed to analyze and interpret the above observational findings with the polarization– intensity gradient method (Koch, Tang & Ho 2012a). Histograms for the field significance Σ_B are shown in the fourth row in Figure 3. Σ_B-maps were previously published in Appendix B in Koch, Tang & Ho (2013) for the CSO sources. For the histograms in Figure 3, a sample-based (IIA, IIB) 3σ-clip is applied to the Σ_B-values in order to remove outliers[7] . Similarly, values below $\Sigma_B \equiv 0.01$ (i.e., 1% field significance) are removed. Both groups of IIA sources show more uniform distributions up to about $\Sigma_B \sim 1$, followed by a rather sharp drop. Type-IIB groups reveal a more exponential-like tail with a significant contribution from the range $\Sigma_B \sim 1-2$. A KS test identifies the two types of distributions as clearly different (CSO IIA versus IIB: $p \sim 10^{-8}$, $k = 0.19$; SMA IIA versus IIB: $p \sim 10^{-11}$, $k = 0.29$). Average values differ with $\langle \Sigma_B \rangle_{IIA} = 0.74$ (SMA) and $\langle \Sigma_B \rangle_{IIB} = 1.49$ (SMA) and $\langle \Sigma_B \rangle_{IIA} = 0.69$ (CSO) and $\langle \Sigma_B \rangle_{IIB} = 1.29$ (CSO). The SMA III sources show an even more pronounced peak at smaller Σ_B-values with $\langle \Sigma_B \rangle = 0.59$. The systematic difference between IIA, IIB and III is also clearly seen in the cumulative distributions with an almost complete absence of values $\Sigma_B > 1$ for III. Thus, the observed differences in $|\delta|$ be-

[7] This does in no way change the shape of the distributions, but it can change average values. A single excessively large Σ_B-value of the order of ~ 100 can significantly boost $\langle \Sigma_B \rangle$ because typical Σ_B-values are of the order ~ 1. We note that outliers are always a consequence of the exponentially growing $\Sigma_B \sim 1/\sin\alpha$ for small angles $\alpha (= \pi/2 - |\delta|)$.

tween the samples IIA and IIB seem to point to a different role of the magnetic field, where Σ_B provides a way to quantitatively discriminate between the samples, identifying IIA ($\langle\Sigma_B\rangle < 1$) and IIB ($\langle\Sigma_B\rangle > 1$) as potentially collapsing and non-collapsing systems on average. The bottom row in Figure 3 illustrates this result with Σ_B-versus-$|\delta|$ plots: IIA sources scatter more densely around smaller $|\delta|$-values, while IIB sources scatter around larger $|\delta|$-values. Type-III sources are even more concentrated around smaller $|\delta|$-values (Table 2).

4.3. Source-Averaged Analysis

From the category-based properties in Section 4.2, we now switch our focus to the analysis of individual sources. Figure 4 displays source-averaged $\langle\Sigma_B\rangle$-values as a function of the source-averaged $\langle|\delta|\rangle$-values. A 3σ-clip is applied to each source separately in Figure 5 in order to calculate $\langle\Sigma_B\rangle$. As a result, IIA sources almost exclusively are found to have $\langle\Sigma_B\rangle < 1$, with $\langle|\delta|\rangle < 40^\circ$. The majority of the IIB sources shows $\langle\Sigma_B\rangle > 1$, with $\langle|\delta|\rangle$ in the range between $\sim 40^\circ$ to $\sim 60^\circ$. This finding is not entirely surprising after the clearly different distributions in Figure 3 for IIA and IIB. Nevertheless, it is not necessarily automatically clear that ensemble-based statistical properties of IIA ($\langle\Sigma_B\rangle_{IIA} < 1$) and IIB ($\langle\Sigma_B\rangle_{IIB} > 1$) also apply to each individual source in each category. It is, thus, rather striking that there seems to be a clear separation between IIA and IIB sources which identifies almost every source with $\langle\Sigma_B\rangle < 1$ as IIA and $\langle\Sigma_B\rangle > 1$ as IIB. Additionally, it is neither obvious from Figure 3 that average $\langle|\delta|\rangle$-values fall strictly on one or the other side of $\langle|\delta|\rangle \approx 40^\circ$.

We have to note that we have limited the above description to the cases that were visually – based on the magnetic field versus source major axis – clearly categorized as either IIA or IIB (red and blue filled symbols in Figure 4 and 5). What about sources that show less obvious patterns with, e.g., incomplete polarization coverages, signs of fragmentation or distorted and less organized field morphologies? The Figures 4 and 5 show $\langle\Sigma_B\rangle$ for all the SMA and CSO sources listed in Table 1, independent of instrument, attempted categorization or physical scale. Ignoring any classification scheme (Table 2), a clear correlation of $\langle\Sigma_B\rangle$ with $\langle|\delta|\rangle$ is seen as well. We stress that no IIA / IIB-categorization is needed to arrive at this result. Our originally proposed distinction between (clear) IIA- and IIB-type sources is based on a crude visual inspection only. Nevertheless, it seems that this simple by-eye assessment is able to fairly reliably distinguish between the two regimes, $\langle\Sigma_B\rangle < 1$ or $\langle\Sigma_B\rangle > 1$ in Figure 4 and 5. In return, this finding indicates: (1) Generally, if magnetic field lines tend to be perpendicular to a clump / core major axis, gravity is dominating on average and overwhelming the magnetic field tension force ($\langle\Sigma_B\rangle < 1$). (2) Generally, if the magnetic field lines tend to be aligned with a clump / core major axis, the magnetic field tension force is on average dominating over gravity. This by-eye inspection is more precisely and quantitatively

assessed with the angle $|\delta|$ which measures the alignment between magnetic field lines and clump / core emission gradients. From Figure 5, the transition between possibly collapsible and non-collapsible systems, on average, occurs at $\langle|\delta|\rangle \approx 40^{\circ}$. Furthermore, it is interesting to note that sources that can not be unambiguously categorized (empty symbols in Figure 4 and 5) also follow the same trend and fit in together with the categorized sources. Additionally, we mark sources that we categorize – again simply by eye – as hourglass-like with a pinched field morphology (type III in our evolutionary scenario) with black filled symbols in Figure 4 and 5. These sources presumably hint collapsing systems in an already more evolved stage (as compared to IIA and IIB). Consistent with that expectation, all these sources show a clearly dominating gravity force with $\langle\Sigma_B\rangle$ around 30% only, together with $\langle|\delta|\rangle \approx 20-30^{\circ}$ which is among the smallest values across the entire sample. Fitting a straight line to all the data (SMA, CSO; type IIA, IIB, III) gives $\langle\Sigma_B\rangle = 0.116 \cdot \exp(0.047 \cdot \langle|\delta|\rangle)$ (Section 5.1).

It is important to stress that $\langle\Sigma_B\rangle$ describes a source-averaged property. In its origin, Σ_B is, nevertheless, a local measurement. Σ_B-maps (Figure 6 and Koch, Tang & Ho (2013)) clearly show distinct zones within the same source where Σ_B can be larger or smaller than one. Thus, for an average $\langle\Sigma_B\rangle > 1$, local collapse with $\Sigma_B < 1$ is still possible. Similarly, $\langle\Sigma_B\rangle < 1$, does not necessarily mean that the entire cloud / core is collapsing.

In conclusion, there are clear and systematic differences in $\langle|\delta|\rangle$ across the sample of 50 sources. This is entirely based on observed magnetic field and dust morphologies only. When interpreting $|\delta|$ in the context of the polarization - intensity gradient method, a clear correlation is found between $|\delta|$ and the significance of the magnetic field. This correlation allows us to discriminate between, on average collapsible and non-collapsible systems. Despite the fact that the SMA ($\theta \sim 1-3''$) and the CSO ($\theta \sim 20''$) are typically probing different scales and densities, there seems to be no difference between the two instruments in Figure 4 and 5. Both the SMA (circles) and the CSO (squares) equally sample sources along the observed range in $\langle|\delta|\rangle$ and $\langle\Sigma_B\rangle$. It is only the type-III sources that were exclusively found among the SMA sample (black filled circles). Further implications of these findings are discussed in Section 5. Finally, a 3σ-clip is applied in Figure 5. This removes only the largest outliers which are typically found in only 1 or 2 locations in a source. As a consequence, the spread in $\langle\Sigma_B\rangle$ is reduced. A clear trend and distinct regimes are already apparent in Figure 4 without any clipping. Table 1 summarizes these values.

5. Discussion

5.1. Magnetic Field Significance $\langle\Sigma_B\rangle$ as Measured from $\langle|\delta|\rangle$

Figure 5 displays source-averaged force ratios (field tension force over gravitational force), $\langle\Sigma_B\rangle$, versus source-averaged $\langle|\delta|\rangle$ (field alignment deviation). The clear observed trend leads to a log-linear best-fit with a scaling $\langle\Sigma_B\rangle = A \cdot \exp(B \cdot \langle|\delta|\rangle)$ with a mean error $d\Sigma_B = \pm 0.20$ and a standard deviation of 0.19 for $A = 0.116$ and $B = 0.047$. *Can we extract any further meaning from exponent and numerical factor in this scaling?* The magnetic field significance $\Sigma_B = \sin\psi / \sin\alpha$ is derived in Koch, Tang & Ho (2012a). α is the complementary angle to the field alignment $|\delta|$, i.e., $\alpha = \pi/2 - |\delta|$ (Figure 1). In the following, we analyze our sample-based scaling for (i) $\langle|\delta|\rangle$ small and (ii) $\langle|\delta|\rangle$ large.

For small angles $|\delta|$, we can write $\langle\Sigma_B\rangle = \langle\sin\psi/\cos|\delta|\rangle \approx \langle\sin\psi\rangle \approx \langle\psi - \psi^3/3! + \cdots\rangle$. ψ is expressed in radians and, if also assumed to be small, it simply becomes $\langle\Sigma_B\rangle \approx \langle\psi\rangle$. On the other hand, expanding the above scaling, $\langle\Sigma_B\rangle \approx A + A \cdot B \cdot \langle|\delta|\rangle + 1/2 \cdot A \cdot B^2 \cdot \langle|\delta|\rangle^2 + \cdots$. Here, $\langle|\delta|\rangle$ is expressed in degree, and the zeroth and first term dominate for small $\langle|\delta|\rangle$. Setting equal the two equations for $\langle\Sigma_B\rangle$, yields $\langle\psi\rangle \approx A + A \cdot B \cdot \langle|\delta|\rangle$. The numerical factor A, thus, sets the limit for the sample's smallest $\langle\psi\rangle$ if $\langle|\delta|\rangle \approx 0$. For the best-fit value $A = 0.116$, $\langle\psi\rangle \approx 7°$. The exponent B (together with A) defines the slope of how $\langle\psi\rangle$ increases across the sample with growing $\langle|\delta|\rangle$. As B is very small, $\langle\psi\rangle$ increases very slowly. For $\langle|\delta|\rangle = 20°$, $\langle\psi\rangle \approx 14°$. Finding small angles $\langle\psi\rangle$ confirms the initial assumption of ψ being small in the above development.

For large $\langle|\delta|\rangle$ we can write $\langle\Sigma_B\rangle = \langle\sin\psi/\cos|\delta|\rangle \approx \sin\psi_s / \langle\cos|\delta|\rangle \approx \sin\psi_s \cdot \langle(1 + |\delta|^2/2 + \cdots)\rangle$, where we assume $\psi \approx const \approx \psi_s$, but still variable from source to source. Higher-order terms in $|\delta|$ are negligible as $|\delta|$ is expressed in radians. In the expansion of the scaling relation, the linear term is negligible, leading to $\langle\Sigma_B\rangle \approx A + 1/2 \cdot A \cdot B^2 \cdot \langle|\delta|\rangle^2$. For the numerical values A and B, the quadratic term further dominates over the zeroth order. Setting equal again the two expressions gives $1/2 \cdot A \cdot B^2 \cdot \langle|\delta|\rangle^2 \approx \sin\psi_s \cdot \langle(1 + |\delta|^2/2)\rangle$. For our numerical values and large $|\delta| \approx 60°$, this yields $\psi_s \approx 20°$. The angle ψ_s grows, to a first order, with $\langle|\delta|\rangle$ but depends on $B^2 = 0.05^2$, which leads again to small values $\langle\psi\rangle$.

We briefly turn our attention to the angle ψ, the difference between emission gradient and (local) gravity direction (Figure 1). $\langle\psi\rangle$ is generally found to be rather small across the entire sample (Figure 7), slowly growing from an average 18° to 35°. In a perfectly symmetric and circular source, emission gradient and gravity direction coincide and $\psi \equiv 0$. More realistically, in close-to-circular, elliptical or still compact systems, ψ still remains small with little variations across the source (as e.g., in W51 e2, IRAS 16293 A, IRAS 16293 B, NGC 1333 IRAS 4A, Orion BN/KL main core, I18360, G34 N, G240...). Our analysis of the scaling relation together with Figure 7 possibly indicates a universal source property with $\langle\psi\rangle$ being generally small. This is

likely a general trend because we are dealing with confined sources (displayed with closed emission contours) that show an accumulation of mass. Overall similar geometries lead to ψ covering similar ranges in each source, consequently leading to a similar spread around similar source-averaged $\langle\psi\rangle$ values.

In summary, linking the sample-based scaling of $\langle\Sigma_B\rangle = A \cdot \exp(B \cdot \langle|\delta|\rangle)$ to the original derivation of Σ_B shows that $\langle\Sigma_B\rangle$ is largely controlled by the source-averaged magnetic field alignment $\langle|\delta|\rangle$. The observed range for $\langle|\delta|\rangle$ is $\sim 17^\circ$ to 60°. For both small and large values in $\langle|\delta|\rangle$, the average emission gradient to gravity misalignment $\langle\psi\rangle$ is estimated to be similar with $\sim 14^\circ$ and $\sim 20^\circ$, respectively. The really observed range grows from $\sim 18^\circ$ to 35°. Thus, $\langle\Sigma_B\rangle$ is indeed influenced to a much smaller extent by $\langle\psi\rangle$. This further supports the interpretation in Koch, Tang & Ho (2013) where, based on the close resemblance between $|\delta|$- and Σ_B-maps, $|\delta|$ was proposed to be a tracer for the change in the magnetic field significance across an observed source.

5.2. Observed $|\delta|$ versus Numerical Study

Morphological imprints in low- to high-magnetization simulated molecular clouds, analyzing relative orientations between magnetic field and column density gradients, were studied in Soler et al. (2013). Their 2D-projected analysis reveals differences in distributions of their angle ϕ (between magnetic field and column density gradients) as a function of magnetization, column density and evolutionary stage. While histograms for low-magnetization cases (weak field strength) peak for all densities and time steps around $\phi \sim 90^\circ$, indicating magnetic fields that are tracing iso-contours in column densities, high-magnetization cases (large field strength) display a shift in distribution peaks as column densities increase from magnetic fields tracing iso-contours to magnetic fields perpendicular to contours (Figure 9 in Soler et al. (2013)). Such opposite trends are precisely seen in our δ-histograms for IIA- vs IIB-type sources (Figure 3). We note that the angle ϕ in Soler et al. (2013) is defined from 0 to 180° where $\phi = 90^\circ$ indicates a magnetic field orientation perpendicular to a column density gradient. We have defined $\delta \in [-90, 90]$ where $\delta = 0^\circ$ means the field is parallel to an emission gradient and ± 90 indicates counter-clock or clockwise rotation. ϕ peaking around 90° is, thus, equivalent to δ peaking around $\pm 90^\circ$ (IIB), and ϕ peaking around 0 and 180° corresponds to a peak in our δ-histograms around 0 (IIA). In the framework of the simulations by Soler et al. (2013), this indicates that IIA sources in both the CSO and the SMA samples are expected to have strongest magnetic fields and largest column densities. This will even more apply to the SMA type-III sources because they show an even more pronounced peak around $\delta \sim 0$. Indeed, large field strength values from a few mG to ~ 10 mG are measured in more evolved, collapsing type-III sources for W51 e2 (Tang et al. 2009b; Koch, Tang & Ho 2012a), G31.41+0.31 (Girart et al. 2009) and NGC 1333 IRAS 4A (Girart et al. 2006). It needs to

be mentioned that IIA/III-type sources having the largest field strengths does not contradict with our finding in Figure 5 where IIA/III-type sources show $\langle\Sigma_B\rangle\lesssim 1$. Σ_B being a ratio, a field strength can significantly increase as material is compressed while, at the same time, a growing gravitational pull from a denser core can still lead to $\Sigma_B\lesssim 1$. The detailed analysis in W51 e2 (Koch, Tang & Ho 2012b) is supporting this picture, revealing growing field strength values from a few mG to about 17 mG in the inner core while Σ_B is indeed decreasing toward the center.

A source-by-source comparison in our sample with the results in Soler et al. (2013) is non-trivial because individual sources often do not have enough independent detected polarization segments in order to unambiguously categorize a δ-histogram according to their classification scheme. We have, therefore, focused on the clearly identified groups IIA, IIB and III in our data sets. By accumulating distributions in this way, we are able to identify differences in δ-distributions that can be matched with numerical results.

5.3. Magnetic Field and Source Orientation

5.3.1. Previous Observational Studies

Tassis et al. (2009) analyzed a sample of 24 molecular clouds, observed in submillimeter dust emission at 350 μm with the CSO/Hertz with a resolution of about 20″ (Dotson et al. 2010). Their study is motivated by the goal to determine the mean orientation of the ordered magnetic field with respect to the cloud principal axes. In their approach they compare the mean dust polarization orientation (derived from all the measured polarization position angles in a cloud) with the cloud aspect ratio (derived from the first and second moments of the dust emission). A statistical treatment, assuming the orientations of the molecular clouds to be random with respect to the line of sight and equally probable, is adopted to overcome projection effects. Tassis et al. (2009) find that oblate cloud shapes are the most likely geometry for their CSO sample while the magnetic field shows a preference to be aligned with the shortest cloud ellipsoidal axis with a deviation of $\sim 24^\circ$ towards the middle and long cloud axes. While their best-fitting distribution is peaking around this value, they note that long tail features are present, and the relatively small number statistics still sets limits to their conclusion. They rule out a scenario where the magnetic field orientations are drawn randomly from a uniform distribution at the percent level.

In a recent study, Li et al. (2013) investigated the orientations of 13 filamentary molecular clouds in the Gould Belt with respect to the intercloud medium (ICM) using near-infrared dust extinction maps and optical stellar polarimetry data. These filaments have low column densities ($\langle A_v\rangle < 2$ mag) with length scales of $\sim 1-10$ pc. Li et al. (2013) define the orientation of a cloud by the long-axis orientation of the auto-correlation function of the column density map. In order

to derive the mean magnetic field orientation of the surrounding ICM (outside of the cloud), an equal-weight Stokes mean of all the detected polarization is adopted. They find that all mean field and cloud orientations fall within 30° from being either perpendicular (7 clouds) or parallel (6 clouds) to each other. They exclude the possibility that such a sample can be drawn from random orientations with a probability of less than 1%. Li et al. (2013) conclude that their finding of a bimodal distribution supports the scenario of a dynamically important magnetic field, disfavoring super-Alfvénic turbulence that would lead to random magnetic field orientations with clouds (e.g., Padoan et al. 2001).

A sample of 14 high-mass star-forming clouds, observed with the SMA in dust polarization at 870μm with a resolution of a few arcseconds, serves as a basis of a statistical analysis in Zhang et al. (2014). The SMA sample typically probes scales around 0.1 to 0.01 pc and densities larger than $10^5 \mathrm{cm}^{-3}$. Zhang et al. (2014) determine the position angle of the clump major axis by fitting a 2-dimensional elliptical Gaussian to the dust continuum emission. The magnetic field orientation over the clump is not averaged but rather for every independent polarization measurement, the absolute difference in angle between the clump major axis and every measured polarization segment is computed. The histogram of these angles reveals a bimodal distribution with two peaks: a first population of magnetic field orientations that is aligned with the clump major axis within about 10°, and a second population associated with magnetic field segments that are perpendicular to the clump major axis within about 40°.

Besides the above summarized studies where polarization is detected across or outside of each cloud or clump with at least several or many independent measurements, earlier studies already probed magnetic field orientations but were limited to a single detection of polarized orientation at the source intensity peak. These studies are summarized in Tassis et al. (2009). The results vary from apparent random orientations with respect to cloud axes (Glenn et al. (1999), 7 elongated cores) to a strong preference of polarized emission aligned with structures (Kane et al. (1993), 6 sources), and magnetic field orientations in cloud cores to be parallel in 3 out of 10 cases (Vallée & Bastien 1999).

5.3.2. $|\delta|$ and Bimodality in Magnetic Field versus Source Orientation?

How do our results for the angle $|\delta|$ (Figures 3 and 5) compare to all the previous studies? The first point to note is that all the earlier work is dealing with samples of only a few up to about 10 sources, with the largest sample being 24 sources in Tassis et al. (2009). Our analysis is based on 50 sources. A second major difference is the analyses and steps taken in order to arrive at the conclusion of aligned or perpendicular fields with respect to a cloud or a core. Essentially every cited work is taking a different approach. This also includes our work here. Further relevant to

these different approaches is the concept of *average* (one single global) quantity versus *local* quantities. Tassis et al. (2009) and Li et al. (2013) compare a single average magnetic field orientation (based on all measured polarization P.A.s and equal-weight Stokes mean of all detected polarization, respectively) with a single average structure orientation (derived from moments aspect ratios and column density auto-correlations, respectively). Zhang et al. (2014) compare a single average source orientation (based on 2-dimensional ellipsoidal fitting) with every independent local magnetic field orientation. Our work here compares every independent local field with every independent local emission gradient orientation. Not only differ all these studies in what they are comparing (average or local quantities), but they also define *average* in different ways. While different data sets can be suggestive for different approaches and different authors can have different preferences, this obviously can introduce biases leading to a non-trivial comparison.

The starting motivations in Koch, Tang & Ho (2012a) to work with *local* quantities was that (1) the role (and strength) of the magnetic field will generally vary with position in a source; and (2) averaging might not always be an adequate operation to characterize certain sources. To be more explicit, for close-to-point symmetrical or close-to-radial field morphologies, as e.g., in W51 e2 (Tang et al. 2009b), defining an average field orientation is not unambiguous. Such systems would typically allow for two possible average orientations with a 90° difference between them. In practise, sources will not be perfectly symmetric. Non-symmetric features, especially if further weighted by, e.g., Stokes *I*, can then tip the balance in favor of one or the other possible average orientation. It is, however, questionable, whether such a subtlety is physically motivated. It is unlikely to provide a robust criterion for such sources. Mathematically, the reason for this ambiguity and complication is the large dispersion between field P.A.s. This is unlike sources that show close-to-uniform field orientations that lead to a small dispersion. A second group of sources where averaging is not well motivated (although it can be computed), are complicated systems, such as, e.g., DR 21(OH) (Girart et al. 2013) where fragmentation and multiple outflows are leading to complex (but still organized) field morphologies. Obviously, one could remedy this situation by simply excluding any questionable sources from any statistical survey studies. We are refraining from that because our goal is to provide a framework to assess the role of the magnetic field in any source. Based on this reasoning, our analysis here is adopting the local quantity $|\delta|$[8]. Despite the differences and complications in comparing the various studies, we are now turning our attention to the question whether there is bimodality in $|\delta|$ or $\langle|\delta|\rangle$ (the source-averaged quantity displayed in Figure 5).

---

[8] An additional property of δ is that it is unambiguously defined in the range -90 to +90° (if giving it a sense of orientation) or 0 to +90° (if working with absolute values). This is because δ and $|\delta|$ are *differences* between 2 P.A.s which makes them rotationally invariant quantities, i.e., they are independent of any reference coordinate. This is unlike P.A.s that are measured with respect to some orientation and reference frame. Additionally, P.A.s suffer from a 180°-ambiguity resulting from the fact that we are measuring orientations only and not directions with vector heads.

Histograms for $\langle|\delta|\rangle$ and $|\delta|$ are shown in Figure 8 for the entire SMA sample and its different categories IIA, IIB and III. As expected, IIA and IIB populate the lower and upper end in the $\langle|\delta|\rangle$-histogram. Type-III sources mostly add to the lower end. Interestingly, some IIA and III sources also fall around $\langle|\delta|\rangle \approx 40°$. The remaining sources – neither classified as IIA, IIB nor III – exclusively fall around mid-values $\sim 40°$. We remark again that the categorization of IIA, IIB and III is simply motivated by visual inspection and does in no way affect the derivation of $\langle|\delta|\rangle$. While there is an indication of a possible bimodality with peaks around $\sim 20°$ and $\sim 55°$ – driven mostly by IIA and IIB sources – the histogram reveals a third peak around $\sim 40°$. *What causes this central peak?* $|\delta|$ very clearly and effectively differentiates between magnetic fields locally aligned or perpendicular to a source structure (emission gradient). Consequently, when calculating an average $\langle|\delta|\rangle$, larger or smaller source major-to-minor axes ratios can lead to a spread around typical IIA and IIB $\langle|\delta|\rangle$-values; e.g., for a source with an axes ratio 3:1 with a magnetic field parallel to its minor axis (type IIA), $\langle|\delta|\rangle$ will be small $\sim 20°$. If the source is less filamentary, becoming more compact and shorter (but still with the field parallel to its minor axis), the axes ratio decreases and $\langle|\delta|\rangle$ will grow to $\sim 30-40°$. Similarly, for IIB-sources where the field is aligned with the source major axis, $\langle|\delta|\rangle$ will decrease as the source becomes less filamentary. All this is simply a result of averaging over more or fewer small (IIA) or large (IIB) $|\delta|$-values because of more or less elongated sources. This then explains a spread in $\langle|\delta|\rangle$, that can populate mid-values. Studies that are comparing mean source orientations versus mean or individual magnetic field orientations (Tassis et al. 2009; Li et al. 2013; Zhang et al. 2014) are less subject to such a spread. The second group falling onto mid-$\langle|\delta|\rangle$ values are sources that are neither categorized as IIA, IIB nor III. Although there are few of these sources, they do exist. In summary, lower- and upper-end peaks in the top panel in Figure 8 can become more pronounced by taking into account spreading in $\langle|\delta|\rangle$ for filamentary sources. This would point toward bimodality. At the same time, nevertheless, there are clearly sources that fall in between. The histogram for the CSO sample reveals a very similar result (Figure 9, top panel), with an upper-end peak that appears more present.

Is there bimodality in $|\delta|$ before averaging? The bottom panels in the Figures 8 and 9 show normalized histograms where $|\delta|$-histograms for each source are normalized to one and then summed up. This normalization removes a possible bias where (nearby) sources with many more independent measurements could dominate the statistics. IIA- and IIB-categories show the expected trends with falling and rising distributions with larger $|\delta|$. This is largely consistent with the histograms in Figure 3 that are counting every single independent measurement. Combining the two categories results in a distribution falling with $|\delta|$. This is further amplified when adding type-III sources for the SMA and non-categorized sources. Assuming that the SMA and CSO samples represent a fair cross-section of star-forming regions, *this result shows that the prevailing source-magnetic field configuration in both the SMA and CSO sample is one that statistically prefers small*

magnetic field misalignments $|\delta|$. With this additional information we might re-interpret the upper panels in Figure 8 and 9: the $\langle|\delta|\rangle$-histograms possibly hint a maximum peak around smallest $\langle|\delta|\rangle$-values with a tail toward larger $\langle|\delta|\rangle$-values. This interpretation is gaining additional support when combining the SMA and CSO samples into one $\langle|\delta|\rangle$-histogram (Figure 10), which shows a broader distribution. $\langle|\delta|\rangle$ is less than 45° in 75% of all the sources. One third of the sources shows $\langle|\delta|\rangle < 30°$. A uniform distribution seems to be ruled out.

We finally note that earlier studies might already have seen hints of such distributions as well. Zhang et al. (2014) suggest a combination of two distributions (0° to 40° and 80° to 90°) with a weight 5:3 to explain their histogram measuring angles between source major axis and polarization orientations. Both Zhang et al. (2014) and Li et al. (2013) state bimodality based on 'fields aligned within 40°' and 'orientations being perpendicular within 30°'. These are wide ranges, given only a 0° to 90° range to fully account for between perfectly aligned and perfectly perpendicular. Bimodality, if at all, is, thus, very unlikely to occur with sharp and narrow peaks. With the to date largest sample of 50 sources it seems to become more plausible that we are dealing with broad distributions peaking at small misalignment values with a tail and a possibly secondary peak or bump toward larger misalignments. With a sample of 24 sources, Tassis et al. (2009) also noticed the presence of long-tail features in their analysis. If further confirmed with even larger samples, this finding would then favor a scenario where the dominating configuration in sources from ∼pc to ∼ mpc scale has the magnetic field roughly aligned with the source minor axis.

On much larger scales (∼ 10′), tracing the interstellar medium (ISM) with polarized dust emission at 353 GHz, recent *Planck* all-sky observations (Planck Collaboration XXXII 2014), investigating the relative orientations between the magnetic field and dust structures, show that in the diffuse ISM structures are preferentially aligned with the magnetic field. A glimpse into denser molecular cloud complexes further reveals that this degree of alignment decreases with increasing column density. The magnetic field tends to become more perpendicular to the interstellar dust ridges, i.e., aligned with their shorter axes. Our results for $|\delta|$ on smaller scales and higher densities agree with this trend.

5.4. Reduced Star-Formation Efficiency and Mass-to-Flux Ratio

Having derived a field significance $\langle\Sigma_B\rangle$ for each source in Figure 4 and 5, we can now proceed to estimate further source properties: star-formation efficiency and mass-to-flux ratio. Since the magnetic field is providing resistance against gravity – quantified with the magnetic field tension-to-gravity force ratio Σ_B – gravity is not everywhere equally effective to initiate and drive a collapse. A concept of magnetic-field-diluted gravity was explored in Shu & Li (1997). With Σ_B we can now define a *gravity efficiency* $\epsilon_G \equiv 1 - \Sigma_B$; i.e., if $\Sigma_B = 0$ or very small, the en-

tire non-diluted gravitational force from an enclosed mass distribution is driving a collapse and the gravity efficiency $\epsilon_G \approx 1$; if Σ_B is large, the magnetic field is holding against gravity and the effectively acting gravity appears reduced with $\epsilon_G < 1$ (Koch, Tang & Ho 2012b). The gravity efficiency is limited to the range between 0 and 1. We set $\epsilon \equiv 0$ if $\Sigma_B > 1$ where collapse is inhibited. The free-fall star-formation efficiency is defined from the free-fall collapse time and mass accretion solving a (pressureless) momentum equation with only a gravitational force term. Absorbing the gravity efficiency factor ϵ_G into an effective gravitational force leads to a magnetic-field-reduced star-formation efficiency (as compared to a free-fall efficiency) $\propto \epsilon_G^{1/2}$ where the square root appears because collapse time is inverse proportional to the square root of the enclosed mass (Koch, Tang & Ho 2012b). Figure 11 displays magnetic-field-reduced star-formation efficiencies, $\langle \epsilon_G^{1/2} \rangle = \sqrt{1 - \langle \Sigma_B \rangle}$, for the entire SMA and CSO samples[9] as a function of $\langle |\delta| \rangle$. The sample-wide trend shows that the magnetic field is able to reduce the star-formation efficiency. Moreover, the efficiency tends to drop with larger $\langle |\delta| \rangle$. The SMA type-III sources show a close-to-maximum efficiency, largely unaffected by the magnetic field. Generally, type-IIB sources reveal a more significantly reduced average efficiency than IIA sources, dropping to 0 ($\langle \Sigma_B \rangle > 1$) and possibly preventing (further) collapse for $\langle |\delta| \rangle \gtrsim 45°$. It is important to note that *local* collapse and *local* star formation are still possible or can be hindered according to the Σ_B-patterns in Figure 6. Sample-averaged efficiencies are around 50%. Finally, it needs to be noted that these reduced efficiencies are upper limits because not all of a cloud's / core's mass might take part in a collapse. This leads to an additional volume efficiency factor, ϵ_V, which can further reduce the total efficiency as $\sim \epsilon_V \cdot \epsilon_G^{1/2}$ (Koch, Tang & Ho 2012b). The conservative estimate here is using $\epsilon_V \equiv 1$.

The second source property we are investigating is the mass-to-flux ratio. Unlike earlier studies (e.g., Crutcher (2012) and references therein) that are relying on a combination of magnetic field strength measurements (like Zeeman line splitting) and a mass proxy to estimate this quantity, we are again making use of the field tension-to-gravity force ratio Σ_B. Explicitly writing out the forces and expressing them in terms of magnetic flux and mass enables us to link Σ_B to the mass-to-flux ratio. The source-averaged mass-to-flux ratio, normalized to the critical mass-to-flux ratio, can be written as $\langle M/\Phi \rangle_{norm} = \langle \Sigma_B^{-1/2} \rangle \cdot \pi^{-1/2}$ (Koch, Tang & Ho 2012b). The inverse square root results from the magnetic flux Φ being proportional to the field strength B whereas the tension force is proportional to $1/B^2$. The numerical factor $\pi^{-1/2}$ appears because magnetic flux is

[9] Here, we are looking for sample-wide trends and, therefore, adopt a source-averaged gravity efficiency $\langle \epsilon_G \rangle$ based on $\langle \Sigma_B \rangle$. It is, nevertheless, worth noting that ϵ_G like the prime observable δ can be locally measured. In Koch, Tang & Ho (2012b), azimuthally averaged gravitational efficiencies $\epsilon_G(r)$ showed clear radial profiles for W51 e2/e8 from several observations, being close to 1 in the core and dropping to $\sim 20\%$ or less in the outer regions.

defined across a cylindrical cross-section πR^2. Normalized mass-to-flux ratios[10] are depicted in the bottom panel in Figure 11 versus $\langle|\delta|\rangle$. The overall result is a mass-to-flux ratio decreasing with larger misalignment angles $\langle|\delta|\rangle$, leaving most of the type-IIA and -III sources in a magnetically supercritical state while most of the type-IIB sources fall below the critical mass-to-flux ratio into a subcritical state. This trend and transition are largely consistent with the scaling of the field significance Σ_B in Figure 5.

6. Summary and Conclusion

A sample of 50 star-forming regions observed in submillimeter dust polarization with the SMA and the CSO is studied with the goal of assessing the significance of the magnetic field. Our analysis is making use of the fundamental observable δ, which is the angle between magnetic field orientation and dust emission gradient. The key results are summarized in the following.

1. Across the entire SMA-CSO-combined sample, $|\delta|$ (from about $4,000$ independent measurements) is populating the entire range between 0 to 90° with a broad peak around smaller values; i.e., the magnetic field is found to range from locally aligned (0°) to locally maximally misaligned (90°) with respect to the dust emission gradient. For this large sample, projection effects likely average out. When interpreting $|\delta|$ with the polarization– intensity gradient method, growing $|\delta|$ generally indicates growing magnetic field significance Σ_B (the ratio of magnetic field tension force to gravity and/or pressure gradient). For local independent measurements, Σ_B can be estimated on average with $\Sigma_B \approx 1/2 \cdot 1/\sin(\pi/2 - |\delta|)$.

2. *Categorization:* Various groups (IIA: tendency of magnetic field to be parallel to source minor axis; IIB: tendency of magnetic field to be parallel to source major axis; III: symmetrized source) show striking differences in group-based $|\delta|$-histograms. Type-IIA and IIB samples depict opposite trends, peaking at small and large $|\delta|$-values, respectively. Type-III sources (only found in SMA observations) peak at even smaller $|\delta|$-values. Sources that can not be categorized, can fall into or in between any of these groups. Group-based differences in $|\delta|$ manifest themselves with clear differences in the group-based field significance: $\langle\Sigma_B\rangle_{IIA}, \langle\Sigma_B\rangle_{III} < 1$ and $\langle\Sigma_B\rangle_{IIB} > 1$.

[10] Analogously to δ and the gravity efficiency ϵ_G, the mass-to-flux ratio based on Σ_B can also be locally computed. A clear transition from magnetically subcritical at larger radii to supercritical towards the core center was found for W51 e2 in Koch, Tang & Ho (2012b). Here, we are again looking for sample-wide trends adopting source-averaged mass-to-flux ratios.

3. *Source-averaged scaling across entire sample:* A clear correlation is found between the source-averaged field misalignment $\langle|\delta|\rangle$ and the source-averaged field significance $\langle\Sigma_B\rangle$. The combined SMA-CSO sample yields a best-fit log-linear scaling $\langle\Sigma_B\rangle = 0.116 \cdot \exp(0.047 \cdot \langle|\delta|\rangle)$ with a mean error $d\Sigma_B = \pm 0.20$. The angle ψ between dust emission gradient and local gravity and/or pressure gradient, which is used in the exact derivation of $\Sigma_B = \sin\psi / \sin\alpha$, shows only small variations across the sample. This explains the tight correlation between $\langle|\delta|\rangle$ and $\langle\Sigma_B\rangle$ and makes $\langle|\delta|\rangle$ a prime observable to trace and quantify the role of the magnetic field. These findings also hold separately for both the SMA and the CSO sources, possibly hinting a scale-free self-similar magnetic field influence. Individual sources that are clearly categorized as IIA (and III) and IIB almost exclusively show average $\langle\Sigma_B\rangle < 1$ (collapse possible, on average) and $\langle\Sigma_B\rangle > 1$ (no collapse, on average). In either case, local collapse can be possible or hindered as Σ_B-maps show distinct zones with Σ_B larger or smaller than one.

4. *Comparison with numerical study:* Numerical simulations of low- to high-magnetization molecular clouds find distributions in δ that can be matched with our observed IIA- and IIB-type segregation. In this framework, IIA- (and III-)type sources represent higher magnetization scenarios with stronger magnetic fields. Large magnetic field strengths are, indeed, measured for, e.g., W51 e2, G31.41+0.31 and NGC 1333 IRAS 4A which are categorized as IIA and III.

5. *Bimodality:* Distributions of the average magnetic field misalignment $\langle|\delta|\rangle$ for the SMA and CSO samples possibly are bimodal. However, combining them together broadens the distributions with a broad maximum peak around small $\langle|\delta|\rangle$-values, a populated mid-range and a secondary smaller peak at larger $\langle|\delta|\rangle$-values. Assuming the SMA and CSO samples to be representative, the most abundant magnetic field-source configuration has, on average, the magnetic field roughly aligned with the emission gradient. This is favoring magnetic fields that are roughly aligned with the source minor axis. 75% of the sources show an average misalignment $\langle|\delta|\rangle$ of less than 45°.

6. *Star-formation efficiency and mass-to-flux ratio:* Based on the field tension-to-gravity force ratio Σ_B, an effectively acting gravitational force can be defined with a gravity efficiency factor $\epsilon_G \equiv 1 - \Sigma_B \leq 1$. Consequently, in the presence of a magnetic field, the standard free-fall collapse time grows and the star-formation efficiency is reduced. The sample-wide trend shows a drop in star-formation efficiency with larger $\langle|\delta|\rangle$ with the average star-formation efficiency being significantly reduced or even suppressed for some sources with $\langle|\delta|\rangle \gtrsim 45°$. Σ_B can also be linked to the normalized mass-to-flux ratio. A transition from magnetically supercritical (mostly for type-IIA and -III sources with small $\langle|\delta|\rangle$) to subcritical (for sources with larger $\langle|\delta|\rangle$) is found across the sample.

The authors thank the referee for valuable comments and suggestions that further improved this manuscript. SPL and TCC are supported by the Ministry of Science and Technology (MoST) of Taiwan with Grant MoST 102-2119-M-007-004-MY3. PMK acknowledges support through grant MoST 103-2119-M-001-009. MP acknowledges the financial support of the OCEVU Labex (ANR-11-LABX-0060) and the A*MIDEX project (ANR-11-IDEX-0001-02) funded by the "Investissements d′Avenir" French government programme managed by the ANR.

REFERENCES

Acord, J.M., Churchwell, E., & Wood, D.O.S. 1998, ApJ, 495, 107

Andersson, B.-G. 2012, arXiv:1208.4393

André, Ph., Di Francesco, J., Ward-Thompson, D., Inutsuka, S., Pudritz, R.E., & Pineda, J., arXiv:1312.6232, accepted for publication as a review chapter in Protostars and Planets VI, University of Arizona Press (2014), eds. H. Beuther, R. Klessen, C. Dullemond, Th. Henning

Anthony-Twarog, B.J. 1982, AJ, 87, 1213

Campbell, M.F., Niles, D., Nawfel, R., Hawrylycz, M., Hoffmann, W.F., & Thronson, H.A., Jr. 1982, ApJ, 261, 550

Cesaroni, R., Churchwell, E., Hofner, P., Walmsley, & C.M., Kurtz, S. 1994, A&A 288, 903

Chapman, N.L., Davidson, J.A., Goldsmith, P.F., et al. 2013, ApJ, 770, 151

Chen, H.-R., Rao, R., Wilner, D.J., & Liu, S.-Y., 2012, ApJ, 751L, 13C

Ciardi, A. & Hennebelle, P. 2010, MNRAS, 409, L39

Crutcher, R.M. 2012, ARA&A, 50, 29

Cudlip, W., Fruniss, I., King, K.J., & Jennings, R.E. 1982, MNRAS, 200, 1169

Davidson, J. A., Novak, G., & Matthews, T. G. et al. 2011, ApJ, 732, 97

Dotson, J.L., Vaillancourt, J.E., Kirby, L., Dowell, C.D., Hildebrand, R.H., & Davidson, J.A. 2010, ApJS, 186, 406

Ewertowski, B. & Basu, S. 2013, ApJ, 767, 33

Frau, P., Galli, D., & Girart, J. M. 2011, A&A, 535A, 44F

Genzel, R., et al. 1981, ApJ, 247, 1039

Genzel, R., Pichon, C., Eckart, A., Gerhard, O.E., & Ott, T. 2000, MNRAS, 317, 348

Girart, J.M., Rao, R., and Marrone, D.P. 2006, Science, 313, 812

Girart, J.M., Beltrán, M. T., Zhang, Q., Rao, R., & Estalella, R. 2009, Science, 324, 1408

Girart, J.M., Frau, P., Zhang, Q., Koch, P.M., Qiu, K., Tang, Y.-W., Lai, S.-P., & Ho, P.T.P. 2013, ApJ, 772, 69

Gonçalves, J., Galli, D., & Girart, J. M. 2008, A&A, 490L, 39G

Glenn, J., Walker, C.K., Young, E.T., 1999, ApJ, 511, 812

Gwinn, C.R., Moran, J.M. & Reid, M.J. 1992, ApJ, 393, 149

Hachisuka, K., Brunthaler, A., Menten, K. M., et al. 2006, ApJ, 645, 337

Hezareh, T., Houde, M., McCoey, C., & Li, H.-b. 2010, ApJ, 720, 603H

Hildebrand, R.H., Dragovan, M., & Novak, G. 1984, ApJ, 284, L51

Hildebrand, R.H. 1988, QJRAS, 29, 327

Hildebrand, R.H., Kirby, L., Dotson, J.L., Houde, M., & Vaillancourt, J.E. 2009, ApJ, 696, 567

Ho, P.T.P., Moran, J.M., and Lo, K.-Y. 2004, ApJ, 616, 1

Houde, M., Vaillancourt, J.E., Hildebrand, R.H., Chitsazzadeh, S., and Kirby, L. 2009, ApJ, 706, 1504

Houde, M., Rao, R., Vaillancourt, J.E., & Hildebrand, R.H. 2011, ApJ, 733, 109

Hull, C.L.H., Plambeck, R.L., Bolatto, A.D., et al. 2013, ApJ, 768, 159

Hull, C.L.H., Plambeck, R.L., Kwon, W., et al. 2014, ApJS, 213, 13

Immer, K., Reid, M. J., Menten, K. M., Brunthaler, A., & Dame, T. M. 2013, A&A, 553, A117

Kane, B.D., Clemens, D.P., Barvainis, R., Leach, R.W., 1993, ApJ, 411, 708

Kataoka, A., Machida, M.N. & Tomisaka, K. 2012, ApJ, 761, 40

Koch, P.M., Tang, Y.-W., & Ho, P.T.P. 2010, ApJ, 721, 815

Koch, P.M., Tang, Y.-W., & Ho, P.T.P. 2012a, ApJ, 747, 79

Koch, P.M., Tang, Y.-W., & Ho, P.T.P. 2012b, ApJ, 747, 80

Koch, P.M., Tang, Y.-W., & Ho, P.T.P. 2013, ApJ, 775, 77

Krasnopolsky, R., Li, Z.-Y., Shang, H., & Zhao, B. 2012, ApJ, 757, 77

Kuchar, T. A., & Bania, T. M. 1994, ApJ, 436, 117

Lai, S.-P., Crutcher, R.M., Girart, J.M., Rao, R. 2001, ApJ, 561, 864L

Lai, S.-P., Crutcher, R.M., Girart, J.M., & Rao, R. 2002, ApJ, 566, 925

Lazarain, A. 2007, JQSRT, 106, 225

Li, H.-b., Dowell, C. D., Kirby, L., Novak, G., & Vaillancourt, J. E. 2008, ApOpt, 47, 422

Li, H.-b, & Houde, M. 2008, ApJ, 677, 1151

Li, H.-b., Fang, M., Henning, T., & Kainulainen, J., 2013, MNRAS, 436, 3707L

Li, Z.-Y., Krasnopolsky, R., & Shang, H. 2013, ApJ, 774, 82

Liu, H.-Y.B., Qiu, K., Zhang, Q., Girart, J.M., & Ho, P.T.P. 2013, ApJ, 771, 71

Loinard, L., Torres, R. M., Mioduszewski, A. J., & Rodríguez, L. F. 2008, ApJ, 675, L29

Machida, M. N., Inutsuka, S., & Matsumoto, T. 2011, PASJ, 63, 555

Mamajek, E.E. 2008, Astron. Nachr., 329, 10

Matthews, B.C., McPhee, C.A., Fissel, L.M., & Curran, R.L. 2009, ApJS, 182, 143

McKee, C.F., & Ostriker, E.C. 2007, ARA&A, 45, 565

Menten, K.M., Reid, M.J., Forbrich, J., & Brunthaler, A. 2007, A&A, 474, 515

Padoan, P., Juvela, M., Goodman, A., & Nordlund Å, 2001, ApJ, 553, 227

Park, B.-G. & Sung, H. 2002, AJ, 123, 892

Pereyra, A., & Magalhães, A.M., 2008, ApJ, 662, 1014

Peretto, N. et al., 2012, A&A, 541, A63

Planck Collaboration XXXII. 2014, arXiv:1409.6728v1

Poidevin, F., Falceta-Goncalves, D., Kowal, G, de Gouveia Dal Pino, E., Magalhaes, A.-M., 2013, arXiv:1309.1047

Povich, M. S. et al. 2007, ApJ, 660, 346

Qiu, K., Zhang, Q., Menten, K.M., Liu, H.-Y.B., & Tang, Y.-W., 2013, ApJ, 779. 182

Racine, R., & van de Bergh, S. 1970, in IAU Symp.38, The Spiral Structure of Our Galaxy, ed. W. Becker & G.I. Contopoulos (Dordrecht:Reidel), 219

Rao, R., Crutcher, R.M., Plambeck, R.L., & Wright, M.C.H. 1998, ApJ, 502L, 75R

Rao, R., Girart, J.M., Marrone, D.P., Lai, S.-P., & Schnee, S. 2009, ApJ, 707, 921

Reid, M.J., Menten, K.M., Xheng, X.W., Brunthaler, A., & Xu, Y. 2009, ApJ, 705, 1548

Rodriguez, L.F., Moran, J.M., Ho, P.T.P., & Gottlieb, E.W. 1980, ApJ, 235, 845

Russeil, D., Zavagno, A., Adami, C. et al. 2012, A&A, 538, A142

Santos, F.P., Franco, G.A.P., Roman-Lopes, A., Reis, W. & Román-Zúñiga, C.G. 2014, ApJ, 783, 1S

Shu, F.H., & Li, Z.-Y. 1997, ApJ, 475, 251

Shu, F.H., Li, Z.-Y., & Allen, A. 2004, ApJ, 601, 930S

Shu, F.H., Galli, D., Lizano, S., & Cai, M. 2006, ApJ, 647, 382

Shinnaga, H., Novak, G., Vaillancourt, J.E. et al., 2012, ApJ, 750, L29

Soler, J.D., Hennebelle, P., Martin, P.G., Miville-Deschênes, M.-A., Netterfield, C.B., & Fissel, L.M. 2013, 774, 128

Stephens, I.W., Looney, L.W., Kwon, W. , et al. 2013 ApJ, 769, L15

Tang, Y.-W., Ho, P.T.P., Girart, J.M., Rao, R., Koch, P.M., & Lai, S.-P. 2009a, ApJ, 695, 1399

Tang, Y.-W., Ho, P.T.P., Koch, P.M., Girart, J.M., Lai, S.-P., & Rao, R. 2009b, ApJ, 700, 251

Tang, Y.-W., Ho, P.T.P., Koch, P.M., & Rao, R. 2010, ApJ, 717, 1262

Tang, Y.-W., Ho, P.T.P., Koch, P.M., Guilloteau, S., & Dutrey, A. 2013, ApJ, 763, 135

Tassis, K., Dowell, C.D., Hildebrand, R.H., Kirby, L., & Vaillancourt, J.E., 2009, MNRAS, 399, 1681

Vallée, J.P., & Bastien, P., 1999, ApJ, 526, 819

Walker, M.F. 1956, ApJS, 2, 365

Xu, Y., Reid, M.J., Zheng, X.W., & Menten, K.M. 2006, Science, 311, 54

Zhang, Q., Qiu, K., Girart, J.M., et al., 2014, ApJ, 792, 116Z

This preprint was prepared with the AAS LaTeX macros v5.2.

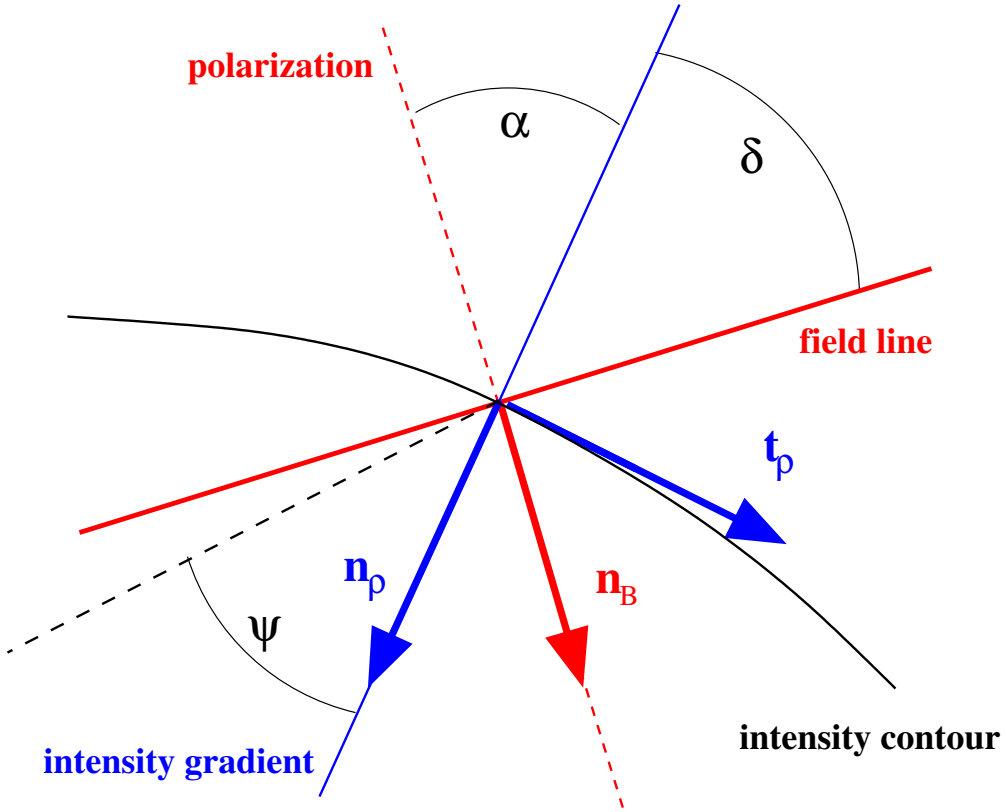

Fig. 1.— Schematic of the relevant angles to calculate the magnetic field significance $\Sigma_B = \sin\psi/\sin\alpha$. The angle δ is measured between magnetic field orientation (red solid line) and intensity gradient orientation (blue solid line), covering the range $0 \leq |\delta| \leq 90°$ or $-90° \leq \delta \leq 90°$ if additionally given a clockwise or counter-clockwise sense of rotation. α is its complementary angle, i.e., $\alpha = \pi/2 - |\delta|$. The magnetic field tension force is directed normal to the field line along the unity vector $\mathbf{n}_B$, collinear to the originally detected dust polarization orientation (red dashed line) which is rotated by 90° with respect to the magnetic field in the case of (sub-)millimeter dust polarization emission. The intensity gradient is normal to the emission intensity contour (black solid line) along the unity vector $\mathbf{n}_\rho \equiv \nabla\rho/|\nabla\rho|$, forming an angle ψ with the (local) gravity and/or pressure gradient orientation (black dashed line). The unity vector tangential to the intensity contour, $\mathbf{t}_\rho$, forms an orthonormal system together with $\mathbf{n}_\rho$. Figure reproduced from (Koch, Tang & Ho 2013).

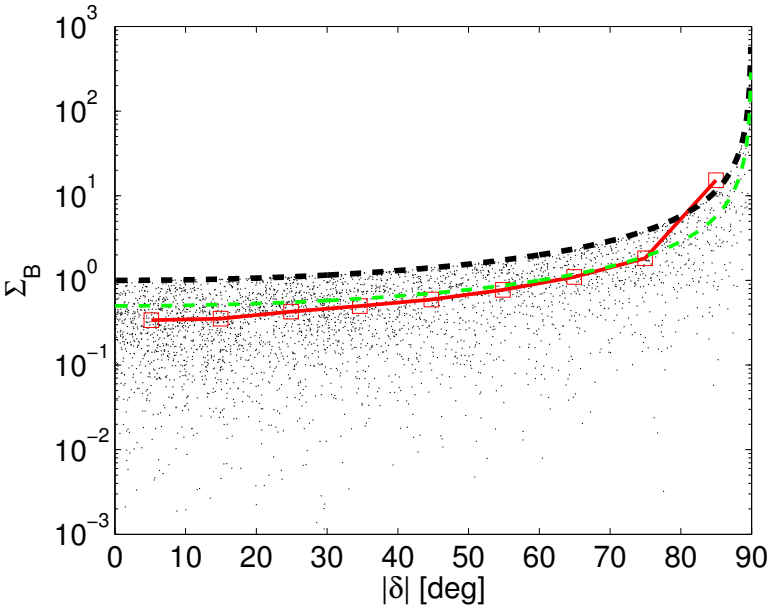

Fig. 2.— Σ_B vs $|\delta|$ for all sources from the combined SMA and CSO samples (close to 4,000 independent $(|\delta|, \Sigma_B)$-pairs). Bin-averaged values are shown with red squares and are connected with straight lines. Values are binned in 10° intervals. The black dashed line shows the upper envelope $1/\sin\alpha \geq 1$. The averaged value in the last bin around 85° falls beyond the upper envelope because of the exponential growth in Σ_B for $|\delta| \to 90°$. The dashed green line is $1/2 \cdot 1/\sin\alpha$.

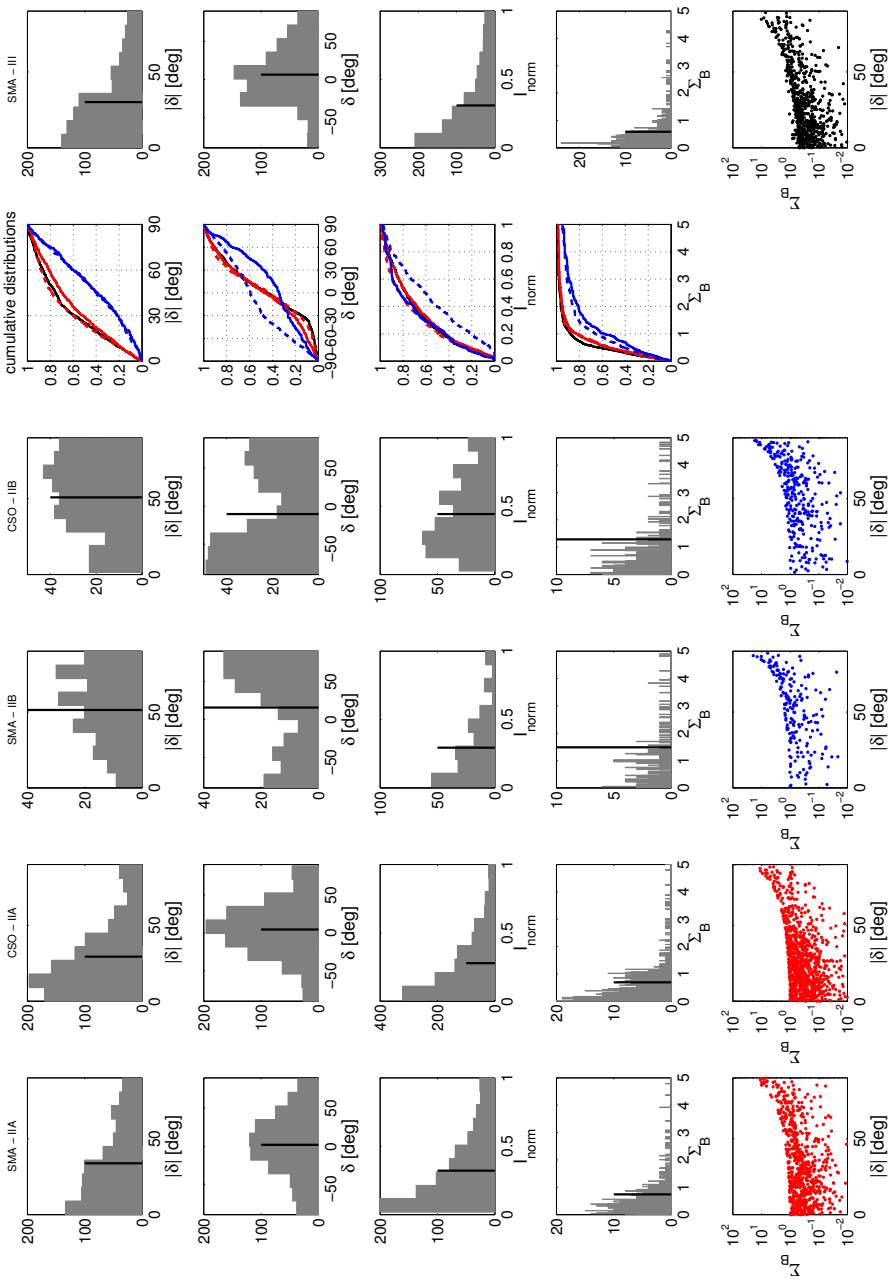

Fig. 3.— Histograms for categorized source groups: the columns one and two are for SMA-IIA and CSO-IIA, columns three and four are for SMA-IIB and CSO-IIB and column six is for SMA-III. Distributions for observed absolute $|\delta|$, relative δ and I_{norm} are shown in the top, second and third row. Clear differences are apparent. Σ_B-histograms, derived from the polarization-intensity gradient method, are displayed in the forth row. Solid vertical lines mark mean values. The bottom row shows scatter plots of Σ_B vs $|\delta|$, illustrating how the different categories fill in different areas in this parameter space. Column five displays cumulative distributions for all the histograms for $|\delta|$, δ, I_{norm} and Σ_B for IIA (red), IIB (blue) and III (black) where solid lines are used for the SMA and dashed lines for the CSO distributions.

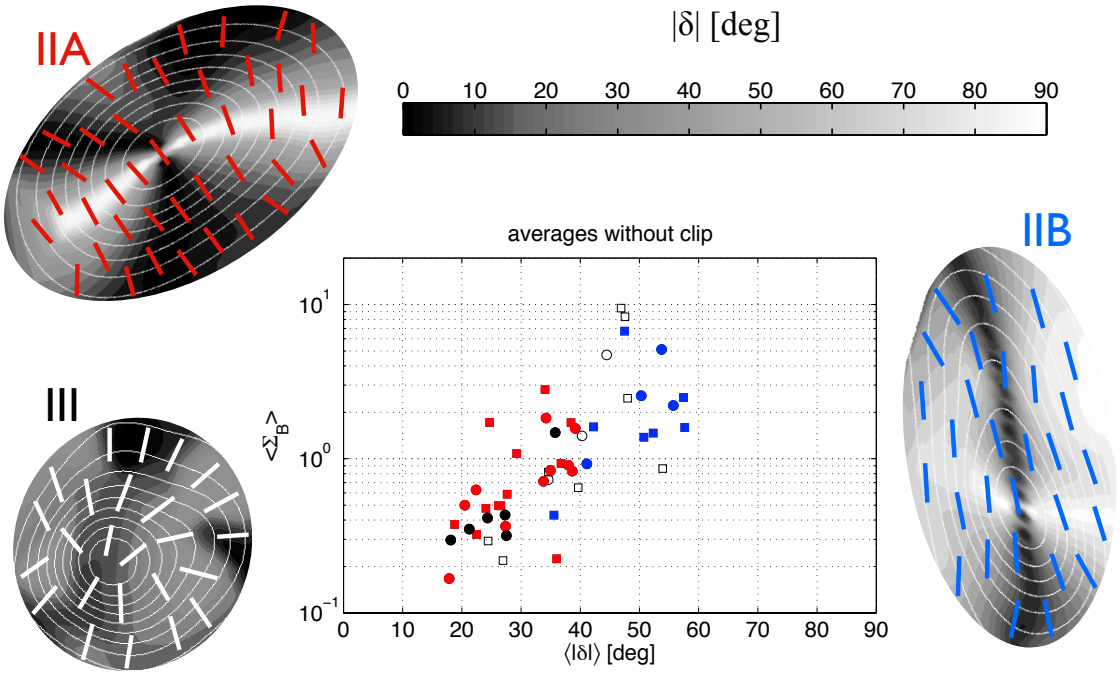

Fig. 4.— Source-averaged $\langle\Sigma_B\rangle$-values vs source-averaged $\langle|\delta|\rangle$-values for the combined SMA and CSO samples. Red and blue filled symbols show the clearly identified IIA- and IIB-type sources from both the SMA (circles) and CSO (squares) sample (Table 1). Empty symbols correspond to sources with less clear features. Black filled circles are the clearly identified SMA-III sources. Averages are calculated including outliers. Schematic magnetic field structures are illustrated for IIA- (red segments), IIB- (blue segments) and III-type sources (white segments). White contours display the dust continuum emission. The black-to-white color grading on the top indicates the local $|\delta|$. Clear opposite trends are apparent for type-IIA and -IIB sources. All 3 schematic types are generated by over-gridding and interpolating really observed sources (IIA, IIB: G240 and G35.2 from Zhang et al. (2014) and Qiu et al. (2013); III: W51 e2 from Tang et al. (2009b)). The systematic local changes in $|\delta|$-maps reflect changes in Σ_B-maps (Koch, Tang & Ho 2013) which explains the observed correlation between $\langle\Sigma_B\rangle$ and $\langle|\delta|\rangle$ across the two samples. Properties for the various source types are summarized in Table 2. Σ_B-maps are shown in Figure 6.

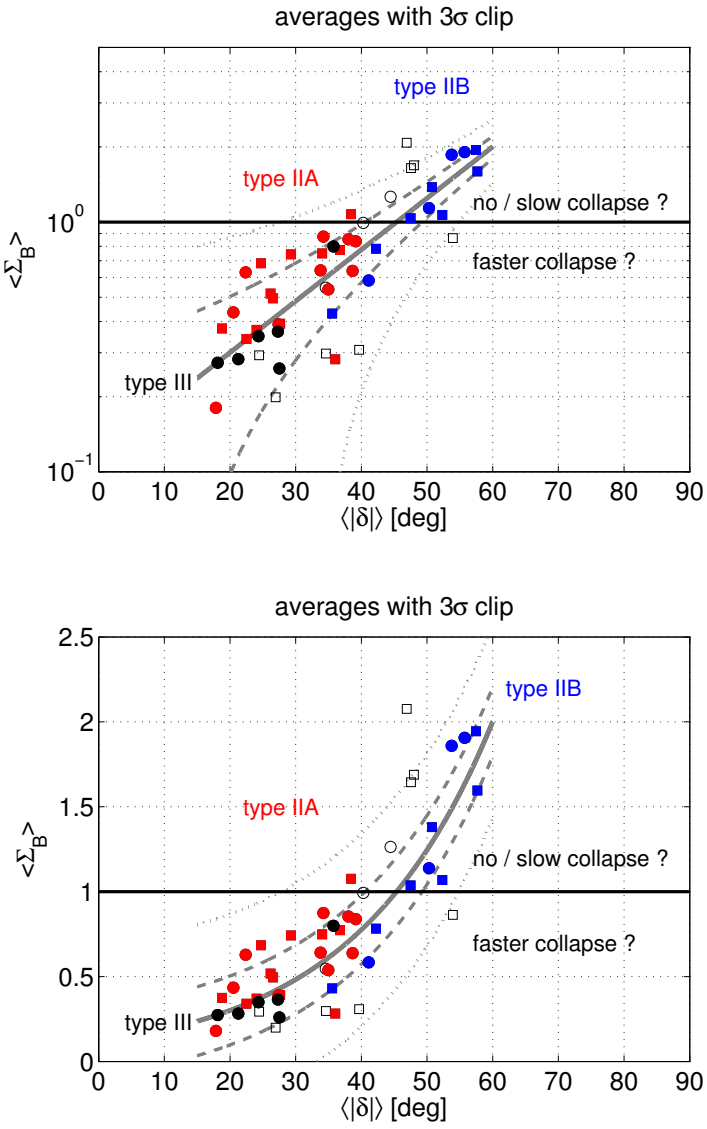

Fig. 5.— Source-averaged $\langle\Sigma_B\rangle$-values vs. source-averaged $\langle|\delta|\rangle$-values for the combined SMA and CSO samples. Different from Figure 4, outliers in Σ_B are removed for each source individually with a 3σ clip. Symbols and colors are identical to the ones in Figure 4. The horizontal line marks the force equilibrium $\langle\Sigma_B\rangle \equiv 1$, below and above which gravity, *on average*, is or is not overwhelming the magnetic field. $\langle\Sigma_B\rangle$ possibly discriminates between systems with, *on average*, no / slow collapse and faster collapse. In either case, *local collapse* and *local star formation* can be possible or hindered as Σ_B-maps show distinct zones with Σ_B larger or smaller than one (Figure 6 and Koch, Tang & Ho (2013)). Clearly identified IIA-type (red) and IIB-type (blue) sources appear to fall onto the left and right side of the transition around $\langle|\delta|\rangle \sim 40°$. The solid gray line is the log-linear best fit $\langle\Sigma_B\rangle = A \cdot \exp(B \cdot \langle|\delta|\rangle)$ with $A = 0.116$ and $B = 0.047$. The dashed and dotted gray lines indicate mean error (± 0.20) and 3σ ($\pm 3 \cdot 0.19$) bounds. The lower panel is identical to the upper panel but in linear-linear scale.

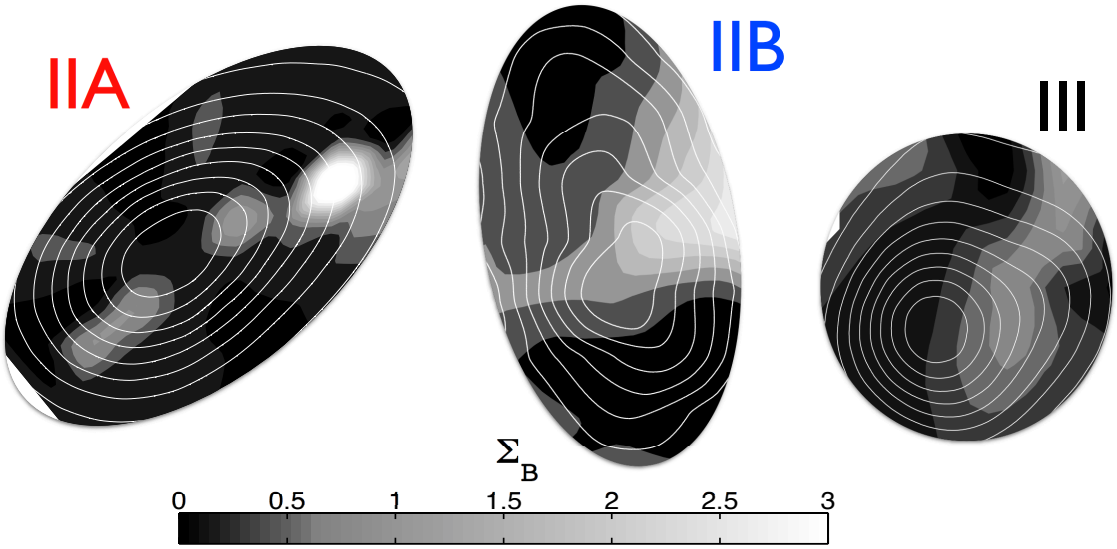

Fig. 6.— Σ_B-maps for the 3 schematic types IIA, IIB and III (Figure 4; IIA, IIB: G240 and G35.2 from Zhang et al. (2014) and Qiu et al. (2013); III: W51 e2 from Tang et al. (2009b)), derived from the effectively observed resolutions listed in Table 1. The black-to-white color grading indicates Σ_B. Corresponding black and white patterns between $|\delta|$ (Figure 4) and Σ_B are visible.

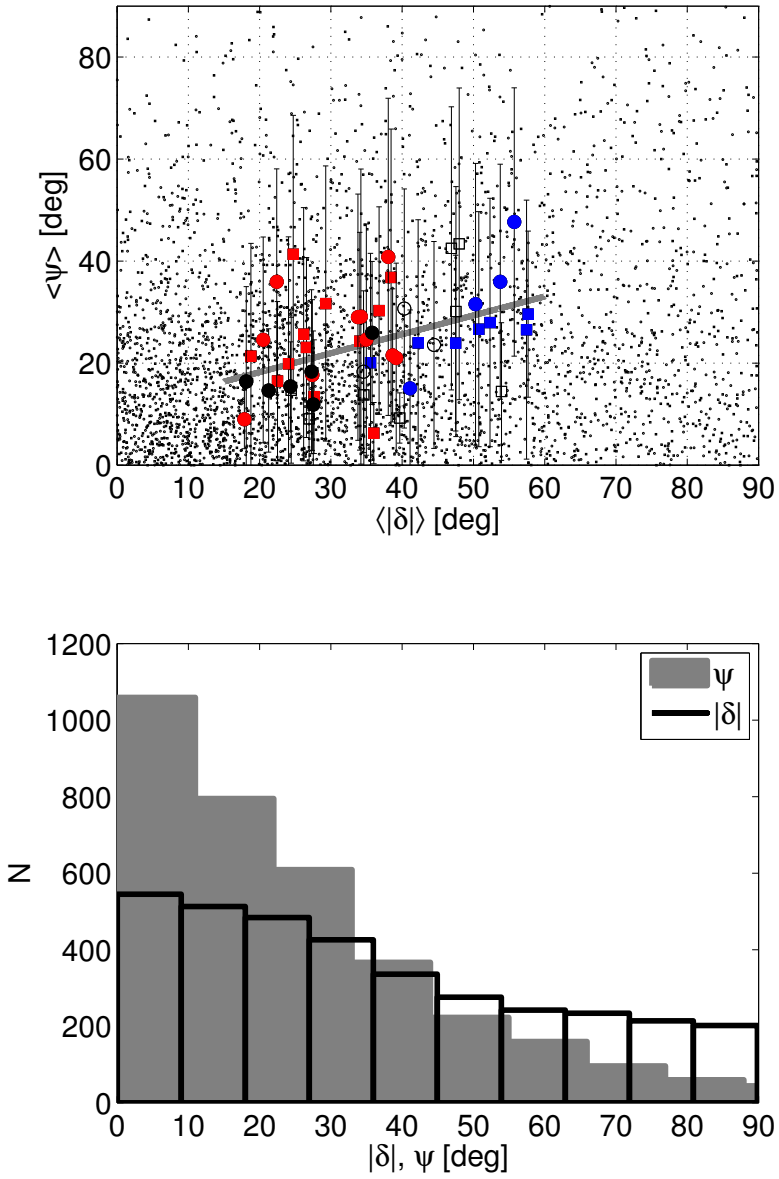

Fig. 7.— Top panel: Source-averaged $\langle\psi\rangle$-values vs source-averaged $\langle|\delta|\rangle$-values for the combined SMA and CSO samples. Symbols and colors are identical to the ones in Figure 4. Vertical lines show the dispersion in ψ for each source. The thick gray line is a linear fit to the averaged values, revealing an only small average increase in $\langle\psi\rangle$ with $\langle|\delta|\rangle$ across the entire sample from $\sim 18°$ to $\sim 35°$. This is significantly less than the change in $\langle|\delta|\rangle$ which makes $\langle|\delta|\rangle$ the main parameter to drive changes in the magnetic field significance Σ_B. Small black dots show all independent $(|\delta|, \psi)$ measurement pairs. Lower panel: Histograms for the SMA-CSO-combined sample for $|\delta|$ and ψ for each measured independent position (not averaged). While $|\delta|$ shows a flatter distribution, ψ is clearly peaked toward small angles. This suggests again rather constant, small values for ψ with minor changes across the sample, as it is found in the upper panel for averaged angles.

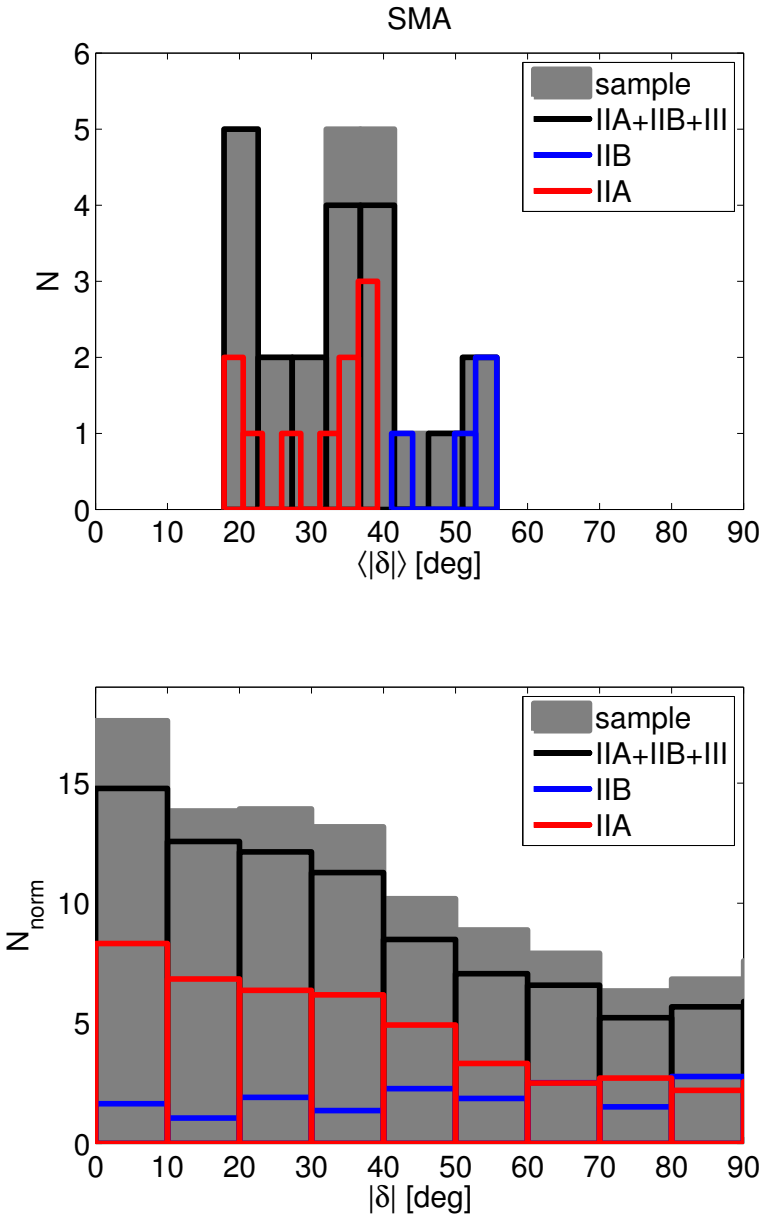

Fig. 8.— Histograms for the SMA sample: source-averaged $\langle|\delta|\rangle$ (top panel) and $|\delta|$ (bottom panel). Bins are slightly shifted in the upper panel for a better display of the various groups. *'Sample'* refers to the entire sample (23 sources) including sources that are not categorized. In the bottom panel, $|\delta|$-histograms for each source are normalized to 1, and then summed up in each bin.

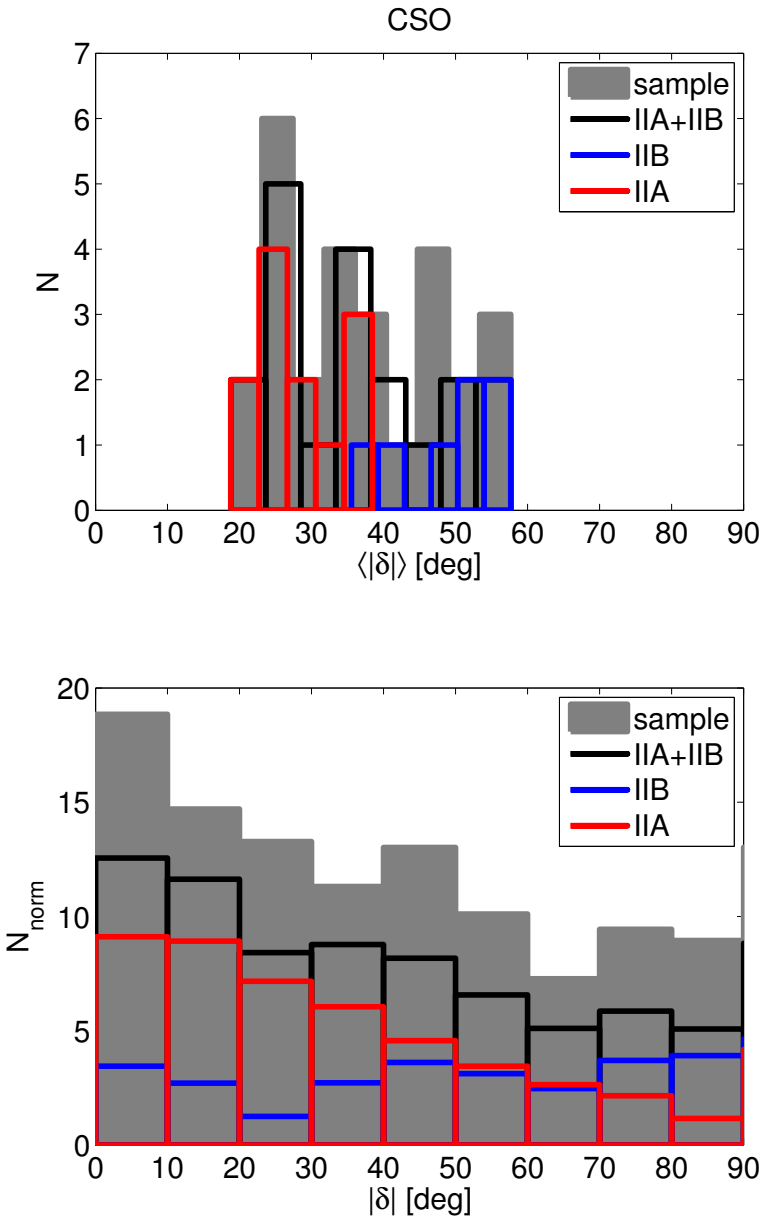

Fig. 9.— Identical to Figure 8 but for the CSO sample. No type-III sources are identified in this sample.

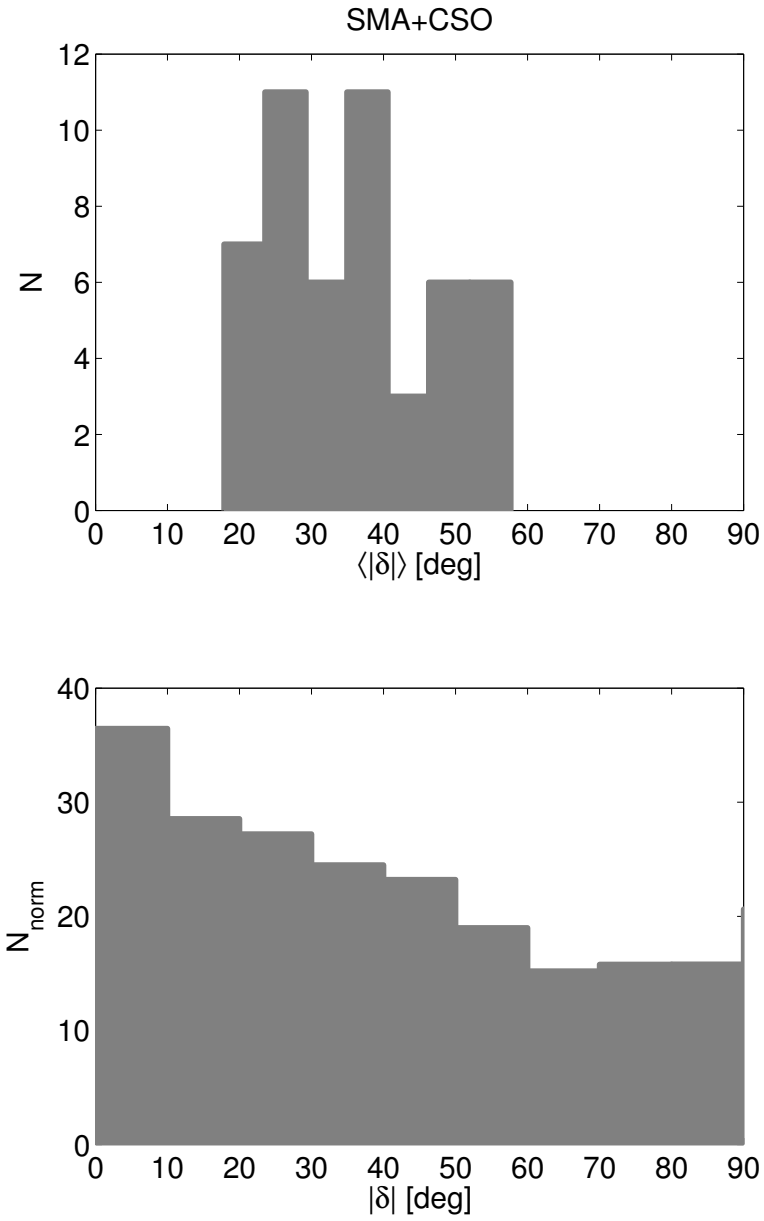

Fig. 10.— Identical to Figure 8 but for the SMA-CSO-combined sample.

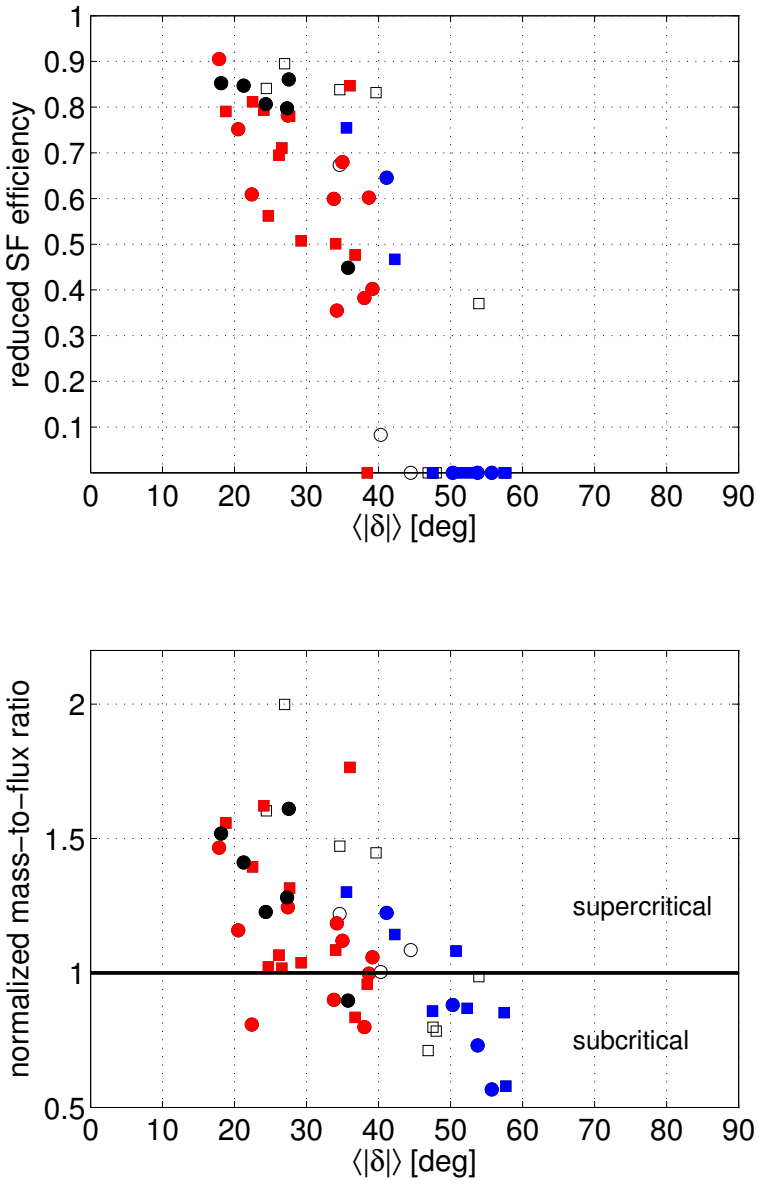

Fig. 11.— Magnetic-field-reduced star formation efficiency (top panel) and normalized mass-to-flux ratio (bottom panel) as a function of source-averaged $\langle|\delta|\rangle$. The solid black line marks the critical mass-to-flux ratio, separating systems that are, *on average*, supercritical or subcritical. In either case, *local collapse* can be hindered or possible according to the schematic $|\delta|$- and Σ_B–patterns in Figure 4 and 6. Symbols and colors are identical to the ones in Figure 4.

Table 1. Analysis Summary

Observation					Analysis									
Source / Region	d (kpc) (1)	λ (μm) (2)	θ ($''$) (3)	ℓ (mpc) (4)	$\mathcal{C}$ (5)	δ_{max} (deg) (6)	δ_{min} (deg) (7)	$<\|\delta\|>$ (deg) (8)	$std(\|\delta\|)$ (deg) (9)	$\Sigma_{B,max}$ (10)	$\Sigma_{B,min}$ (11)	$<\Sigma_B>$ (12)	$std(\Sigma_B)$ (13)	Phase (14)
SMA														
G240	4.7	870	2.1	48	0.81	83	-83	24	23	1.62 (3.71)	0.02 (0.02)	0.35 (0.41)	0.30 (0.52)	III
G34.4.0	1.57	870	1.5	11	0.93	87	-61	28	23	1.16 (4.27)	0.01 (0.001)	0.26 (0.32)	0.25 (0.54)	III
G34.4.1	1.57	870	1.5	11	0.42	89	-89	34	25	10.6 (54.8)	0.02 (0.007)	0.87 (1.84)	1.66 (6.55)	IIA
G35.2	2.19	870	1.5	16	0.63	90	-87	54	24	19.4 (194)	0.02 (0.02)	1.86 (5.11)	3.22 (25.2)	IIB
NGC 6334A	1.7	870	5.2	43	0.60	84	-84	56	21	8.96 (10.3)	0.19 (0.19)	1.91 (2.22)	1.99 (2.53)	IIB
NGC 6334I	1.7	870	1.5	12	0.81	82	-90	50	23	10.1 (136)	0.02 (0.003)	1.14 (2.56)	1.42 (14.0)	IIB
NGC 6334IN	1.7	870	2.4	20	0.81	79	-87	38	27	2.52 (3.93)	0.04 (0.04)	0.85 (0.91)	0.52 (0.65)	IIA
NGC 6334V	1.7	870	2.9	24	0.78	79	-89	39	24	12.5 (49.5)	0.02 (0.01)	0.84 (1.57)	1.86 (6.35)	IIA
I 18360	4.8	870	1.6	37	0.70	89	-86	41	28	3.95 (6.07)	0.04 (0.04)	0.58 (0.93)	0.98 (1.66)	IIB
DR 21(OH)	1.7	870	1.3	11	0.74	88	-87	40	26	7.04 (21.8)	0.02 (0.007)	0.99 (1.41)	1.30 (2.73)	-
g5.89 *	2	870	2.4	23	0.72	76	-84	35	26	2.88 (8.34)	0.01 (0.008)	0.55 (0.73)	0.66 (1.41)	-
Orion BN/KL *	0.48	870	2.8	6.4	0.70	89	-90	44	25	30.4 (136)	0.02 (0.002)	1.26 (4.72)	3.99 (20.1)	-
W51 e2 - ext *	7	870	0.7	24	0.95	33	-47	18	12	1.26 (1.35)	0.02 (0.007)	0.27 (0.30)	0.30 (0.33)	III
W51 e2 - sub+comp	7	870	2.0	68	0.92	77	-34	18	16	0.35 (0.35)	0.06 (0.002)	0.18 (0.17)	0.09 (0.10)	IIA/III
W51 e8 - sub+comp	7	870	2.0	68	0.76	85	-74	22	22	1.35 (1.35)	0.12 (0.12)	0.63 (0.63)	0.31 (0.31)	IIA/III
W51 e2+e8 - sub+comp	7	870	2.0	68	0.84	85	-74	21	20	2.0 (2.57)	0.02 (0.02)	0.44 (0.50)	0.36 (0.51)	IIA/III
W51 North - ext *	7	870	0.7	24	0.89	82	-81	34	23	2.48 (4.37)	0.03 (0.005)	0.64 (0.71)	0.54 (0.79)	IIA/III
W51 North - sub+comp	7	870	2.0	68	0.90	70	-53	27	15	1.25 (1.25)	0.03 (0.003)	0.39 (0.36)	0.31 (0.32)	IIA
NGC 1333 IRAS4A *	0.3	870	1.2	1.7	0.82	84	-89	27	19	1.43 (4.27)	0.01 (0.002)	0.36 (0.43)	0.29 (0.58)	IIA/III
IRAS 16293 A *	0.12	870	2.5	1.5	0.86	90	-86	36	23	10.1 (177)	0.02 (0.004)	0.80 (1.48)	1.08 (9.66)	III
IRAS 16293 B *	0.12	870	2.5	1.5	0.57	89	-90	39	25	3.92 (10.1)	0.01 (0.006)	0.64 (0.83)	0.60 (1.35)	IIA/III
G31.41 *	7.9	870	0.9	34	0.92	73	-82	21	21	1.30 (3.83)	0.01 (0.05)	0.28 (0.35)	0.23 (0.51)	III
W3 (OH)*	2.04	870	1.5	15	0.79	77	-87	35	22	2.50 (7.74)	0.02 (0.001)	0.54 (0.84)	0.57 (1.64)	IIA
CSO														
CO+0.02/ M−0.02	7.9	350	20	770	0.71	89	-88	48	25	13.9 (54.1)	0.02 (0.02)	1.69 (2.47)	2.21 (5.97)	I/-
Mon R2	0.95	350	20	92	0.78	67	-55	23	18	1.17 (1.17)	0.01 (0.005)	0.34 (0.32)	0.29 (0.29)	IIA
M+0.25+0.01	7.9	350	20	770	0.61	88	-89	57	24	13.0 (38.6)	0.01 (0.005)	1.83 (2.41)	2.88 (5.64)	IIB
NGC 2068 LBS10	0.4	350	20	39	0.62	77	-84	51	24	5.33 (5.33)	0.02 (0.02)	1.38 (1.38)	1.67 (1.67)	IIB
NGC 2024	0.4	350	20	39	0.55	85	-85	37	24	4.26 (7.17)	0.05 (0.05)	0.77 (0.93)	0.83 (1.30)	IIA

Table 1—Continued

Observation					Analysis									
Source / Region	d (kpc) (1)	λ (μm) (2)	θ ($''$) (3)	ℓ (mpc) (4)	$\mathcal{C}$ (5)	δ_{max} (deg) (6)	δ_{min} (deg) (7)	$<\|\delta\|>$ (deg) (8)	$std(\|\delta\|)$ (deg) (9)	$\Sigma_{B,max}$ (10)	$\Sigma_{B,min}$ (11)	$<\Sigma_B>$ (12)	$std(\Sigma_B)$ (13)	Phase (14)
NGC 2264	0.8	350	20	78	0.94	42	-67	36	18	1.36 (1.36)	0.03 (0.03)	0.43 (0.43)	0.46 (0.46)	IIB
NGC 6334A	1.7	350	20	170	0.84	86	-86	28	26	2.89 (7.27)	0.06 (0.002)	0.39 (0.59)	0.54 (1.31)	IIA
G34.3+0.2	3.7	350	20	360	0.87	89	-85	35	24	0.98 (17.8)	0.01 (0.007)	0.30 (0.82)	0.22 (3.06)	IIB
ρ Oph	0.139	350	20	14	0.66	88	-78	27	24	1.02 (1.02)	0.03 (0.03)	0.50 (0.50)	0.31 (0.31)	IIA
W49 A	11.4	350	20	1110	0.86	77	-65	27	22	0.59 (1.02)	0.02 (0.004)	0.20 (0.22)	0.18 (0.25)	-
GGD12	1.7	350	20	170	0.98	56	-18	24	16	0.85 (0.85)	0.02 (0.02)	0.29 (0.29)	0.29 (0.29)	-
NGC 6334I	1.7	350	20	170	0.63	88	-84	38	25	9.20 (34.9)	0.01 (0.01)	1.08 (1.71)	1.46 (4.87)	IIA
M+0.34+0.06	8	350	20	780	0.81	71	-83	58	26	5.06 (5.06)	0.39 (0.39)	1.60 (1.60)	1.56 (1.56)	IIB
W33 C	2.4	350	20	230	0.74	89	-75	40	27	1.09 (7.48)	0.02 (0.02)	0.31 (0.65)	0.30 (1.59)	-
W33 A	2.4	350	20	230	0.87	80	-75	36	22	1.17 (1.17)	0.01 (0.003)	0.28 (0.22)	0.35 (0.33)	IIA
M 17	1.6	350	20	160	0.44	88	-90	34	26	7.18 (149)	0.01 (0.01)	0.75 (2.81)	1.12 (15.9)	IIA
W3	1.95	350	20	190	0.91	78	-81	24	23	1.72 (3.01)	0.01 (0.002)	0.37 (0.48)	0.42 (0.67)	IIA
OMC 1	0.414	350	20	40	0.59	86	-90	29	20	11.2 (74.3)	0.01 (0.001)	0.74 (1.08)	1.09 (4.50)	IIA
OMC 3	0.414	350	20	40	0.59	59	-89	25	20	1.57 (31.7)	0.02 (0.02)	0.68 (1.72)	0.42 (5.68)	IIA
Sgr A* East	8	350	20	780	0.83	90	-90	47	30	14.1 (138)	0.04 (0.04)	2.08 (9.48)	3.09 (30.0)	I/-
IRAS 05327	0.414	350	20	40	0.43	81	-88	54	28	2.77 (2.77)	0.11 (0.11)	0.86 (0.86)	0.92 (0.92)	-
Sgr B2	8	350	20	780	0.70	90	-87	52	21	11.5 (63.0)	0.02 (0.001)	1.07 (1.47)	1.46 (5.22)	IIB
Sgr B1	8	350	20	780	0.76	90	-90	48	28	36.3 (204)	0.06 (0.06)	1.64 (8.33)	4.94 (35.5)	I / IIA
DR21	3	350	20	290	0.58	86	-87	26	22	1.74 (3.61)	0.01 (0.001)	0.52 (0.50)	0.37 (0.52)	IIA
Mon OB1 IRAS 12	0.80	350	20	78	0.65	88	-88	42	29	5.56 (17.2)	0.01 (0.01)	0.78 (1.61)	1.17 (3.74)	IIB
M–0.13−0.08	8	350	20	780	0.71	90	-80	47	29	3.32 (123)	0.07 (0.006)	1.04 (6.73)	0.98 (26.6)	IIB
M+0.07−0.08	8	350	20	780	0.89	38	-37	19	11	1.02 (1.02)	0.01 (0.01)	0.37 (0.37)	0.38 (0.38)	IIA

Note. — Examples of $|\delta|$- and Σ_B-maps are shown in Koch, Tang & Ho (2013) for CSO sources. Values in parentheses for $\Sigma_{B,max}$, $\Sigma_{B,min}$, $\langle\Sigma_B\rangle$ and $std(\Sigma_B)$ represent values before removing statistical outliers with a 3σ clip. Some values differ slightly from the ones in Koch, Tang & Ho (2013) due to the way outliers were handled. Sources with "*" were previously observed outside of the SMA polarization legacy program. *ext, sub* and *comp* refer to the SMA extended, subcompact and compact array configurations. Results for W51 e2, e8 and North are listed separately for different configurations as they are sampling different physical scales such as envelope or core (Tang et al. 2013). Source coordinates of the original observations are listed in Dotson et al. (2010) and Zhang et al. (2014).

[(1)]Source distance. Values are from Genzel et al. (1981) for W51 and Orion BN/KL, Acord et al. (1998) for g5.89, Racine & van de Bergh (1970) for Mon R2 and from Reid et al. (2009) for CO+0.02−0.02 / M–0.02−0.07 and M+0.25+0.01. Further: NGC 2068 LBS10 and NGC 2024 (Anthony-Twarog 1982), NGC 2264 (Park & Sung 2002), NGC 6334A and 6334I (Russeil et al. 2012), G34.3+0.2 (Kuchar & Bania 1994), ρ Oph (Mamajek 2008), W49 A (Gwinn et al. 1992), GGD12 (Rodriguez et al. 1980), sources around the galactic center, i.e.,

M+0.34+0.06, Sgr A* East, Sgr B2, Sgr B1, M–0.13–0.08, M+0.07–0.08 (Genzel et al. 2000), W33 C and W33 A (Immer et al. 2013), M17 (Povich et al. 2007), W3 (Xu et al. 2006), OMC 1, OMC 3 and IRAS 05327 (Menten et al. 2007), DR21 (Campbell et al. 1982), Mon OB1 IRAS 12 (Walker 1956), IRAS 16293 (Loinard et al. 2008), G31.41 (Cesaroni et al. 1994), W3(OH) (Hachisuka et al. 2006).

(2)Observing wavelength.

(3)Beam resolution. For elliptical beams (synthesized beams of the SMA) the geometrical mean is adopted. For Hertz/CSO, the nominal beam size of $\sim 20''$ is listed.

(4)Physical size scales at the source distances for the resolutions θ.

(5)Correlation coefficient in the definition of Pearson's linear correlation coefficient between magnetic field *P.A.*s and the intensity gradient *P.A.*s.

(6)Maximum difference between magnetic field and intensity gradient orientation.

(7)Minimum difference between magnetic field and intensity gradient orientation.

(8)Mean absolute difference between magnetic field and intensity gradient orientations.

(9)Standard deviation of absolute differences.

(10)Maximum magnetic field significance.

(11)Minimum magnetic field significance.

(12)Mean magnetic field significance.

(13)Standard deviation of magnetic field significance.

(14)Assigned phase (I, IIA, IIB, III) according to the schematic scenario in Figure 11 in Koch, Tang & Ho (2013). No phase is assigned to DR21(OH) (fragmenting core with multiple outflows (Girart et al. 2013)), g5.89 (probably in a later more evolved stage with expanding HII regions (Tang et al. 2009a)) and Orion BN/KL (explosive outflow or pseudodisk (Tang et al. 2010)).

Table 2. Source Type Properties

Type	Dust Morphology	Magnetic Field-Source Morphology	$\lvert\delta\rvert$ and Σ_B
I	irregular	irregular	irregular
IIA	elongated	field mostly aligned with source minor axis	systematic: overall small, larger towards and along central major axis
IIB	elongated	field mostly aligned with source major axis	systematic: overall large, smaller towards and along central major axis
III	more circular	field increasingly radial and / or hourglass-like	systematic: overall small, additional azimuthal symmetries in $\pm\delta$

Note. — Examples for IIA, IIB and III are shown in Figure 4 and 6. Additional azimuthal symmetries appear in $\pm\delta$ (when giving it a sense of orientation) for type-III sources due to pinched magnetic field lines (Figure 6 in Koch, Tang & Ho (2013)). Type-I sources are precursors where $|\delta|$- and Σ_B-properties are not yet clearly established.